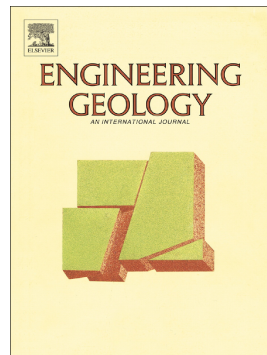


Journal Pre-proof

Numerical investigation of debris flows using a two-phase continuum model incorporating a visco-inertial rheology



Yunxu Xie, Gordon G.D. Zhou, Kahlil F.E. Cui, Xueqiang Lu

PII: S0013-7952(22)00282-4

DOI: <https://doi.org/10.1016/j.enggeo.2022.106797>

Reference: ENGEO 106797

To appear in: *Engineering Geology*

Received date: 7 December 2021

Revised date: 12 July 2022

Accepted date: 23 July 2022

Please cite this article as: Y. Xie, G.G.D. Zhou, K.F.E. Cui, et al., Numerical investigation of debris flows using a two-phase continuum model incorporating a visco-inertial rheology, *Engineering Geology* (2022), <https://doi.org/10.1016/j.enggeo.2022.106797>

This is a PDF file of an article that has undergone enhancements after acceptance, such as the addition of a cover page and metadata, and formatting for readability, but it is not yet the definitive version of record. This version will undergo additional copyediting, typesetting and review before it is published in its final form, but we are providing this version to give early visibility of the article. Please note that, during the production process, errors may be discovered which could affect the content, and all legal disclaimers that apply to the journal pertain.

Numerical investigation of debris flows using a two-phase continuum model incorporating a visco-inertial rheology

Yunxu Xie¹, Gordon G.D. Zhou^{*1,2,3}, Kahlil F. E. Cui^{1,2}, Xueqiang Lu^{1,2}

¹ Key Laboratory of Mountain Hazards and Earth Surface Process / Institute of Mountain Hazards and Environment, Chinese Academy of Sciences, Chengdu 610000, China

² University of Chinese Academy of Sciences, Beijing 100000, China

³ China-Pakistan Joint Research Center on Earth Sciences, CAS-HEC

Corresponding author: Gordon G.D. Zhou (gordon@imde.ac.cn),

Highlights:

- Debris flows are simulated as two-phase flows where the solid phase is modelled using a visco-inertial constitutive rheology.
- The numerical model captures the enhanced mobility and phase separation in debris flows.
- Simulations with visco-inertial model improves predictions against dry granular flow rheology.

Abstract: The motion of debris flows is controlled by the interaction of their fluid and solid components. In this work, a general two-phase model framework (Pudasaini 2012) is adopted which captures the coupled effects of the individual phase dynamics to the overall mobility. While solving the model equations, the fluid phase is treated as a viscous Newtonian liquid while the solid phase is considered to be a granular material obeying a recently developed visco-inertial constitutive rheology. Solid and fluid components in the mixture are coupled through the interaction forces, namely buoyancy, drag, and virtual mass. The model is calibrated against results from instrumented flume experiments and from field measurements of saturated, channelized debris flows. The numerical model captures the enhanced mobility of debris flows due to the presence of interstitial fluid and provides better predictions of the flow dynamics relative to those obtained from single-phase frameworks. Better modeling agreement is obtained for granular-fluid flows with relatively high fluid content. The model is then used to simulate real debris flow events, including a case that occurred in the proximity of the Sichuan-Tibet Railway, where good agreement with reported field measurements is obtained. This modeling framework is expected to improve mitigation strategies for debris flows hazards.

Keywords: Sichuan-Tibet Railway; Sichuan-Tibet Highway; Two-phase model; Visco-inertial rheology

1 Introduction

Debris flows are destructive, multiphase, gravity-driven flows consisting of solid and fluid phases that mix and interact with each other as they surge down inclined slopes (Iverson 1997; Iverson and Denlinger 2001; Pudasaini et al. 2005). They consist of broad grain size distributions and often include a viscous interstitial fluid. Constituent particle sizes may range from several meters (e.g. boulders or rock clasts) to micrometers (e.g. fine silt and clay) (Iverson 1997). The fluctuations and interactions of the larger particles control the inertial motion of debris flow while the fine particles mix with the pore fluid to form viscous muddy suspensions. Shear-induced particle re-arrangement generates transient excess pore water pressures (Iverson and LaHusen 1989) and the drag (Pudasaini 2020) that influences the fluid phase velocity. On the other hand, the buoyant force resulting from the presence of fluid reduces the amount of energy dissipated

from particle collisions which may also contribute to enhanced bulk flow mobility (Pitman and Le 2005; Pudasaini 2012). The individual and coupled dynamics of the solid and fluid phases make the kinetic behaviors of debris flow distinct from those of other geophysical mass flows (Iverson 1997). It is essential to understand the improved mobility (Pudasaini and Krautblatter 2014, 2021) resulting from these phase interactions to make reliable predictions of their dynamic behaviors.

In previous works, debris flows have been modeled as dry single-phase phenomena (Savage and Hutter 1989; Hungr 1995; Iverson 1997; Iverson and Denlinger 2001; Pudasaini and Hutter 2003; Patra et al. 2005; Liu et al. 2016) wherein a single set of mass and momentum balance laws are solved to quantitatively describe the temporal and spatial evolution of their dynamics (Hungr 1995; Pudasaini et al. 2005; Ouyang et al. 2015). This modeling framework disregards the effects of the presence of interstitial fluids which are known to influence individual particle motion (Cui et al. 2020) and debris flows' overall mobility (De Haas et al. 2015). To remedy this, later modeling strategies incorporated a fluid constitutive stress component into the single-phase flow framework (Pitman and Le 2005; Fernández-Nieto et al. 2008; Liu et al. 2016). However, simply adding two empirical or semi-empirical constitutive laws cannot sufficiently model the coupled dynamics of the two phases. An alternative is to use extra constitutive equations for pore water pressure that can define the generation and the dissipation of pore fluid pressure and therefore incorporate the viscous effects acting on the solid phase (George and Iverson 2014; Iverson and George 2014). However, the physical relevance of such modeling strategies is incomplete since they are unable to account for the interfacial interactions resulting from the relative motion of the solid particles and the ambient fluid. Despite these limitations, single-phase models are still widely used since they are able to adequately capture first-order dynamics of most two-phase flows and require lesser computational cost.

Recently, debris flows and many other complex catastrophic mass follow events are dominantly being simulated by using multi-phase mass flow models by (Pudasaini 2012) and (Pudasaini and Mergili 2019), e.g., Kattel et al. (2016); Kafle et al. (2019); Qiao et al. (2019); Mergili et al. (2020a); Mergili et al. (2020b); Shugar et al. (2021). In contrast to single-phase models, multi-phase flow models solve separate equations of motion for the solid and fluid constituents and hence enable the calculation of interfacial stresses between phases

(Pudasaini 2012; Bouchut et al. 2016). Modeling interfacial interactions require constitutive models for momentum transfer between solid and fluid phases, e.g., buoyancy, viscous drag, and virtual mass forces in a particle-fluid flow system. Drag is one of the basic mechanisms of two-phase flows as it incorporates coupling between the phases. The drag can vary substantially depending on the flow dynamics and the concentration of particles. The model of (Pudasaini 2012) adopted a generalized drag law that was derived based on the terminal velocity of a freely falling sphere in fluid, and from the velocity of fluids flowing through porous media. Pudasaini (2020) further improved the drag model to cover a wider range of particle concentrations without any singularities. Aside from the viscous drag, the virtual mass force plays an important role in the dynamics of solid-fluid mixture flows. When a particle moves through fluid, it drags the surrounding fluid to motion. The acceleration resulting from the fluid motion increases to match the particle velocity leading to a virtual increase in the particle mass (Pudasaini 2012). In Pudasaini (2019), the virtual mass model is extended in such a way that it is smooth enough and well-bounded for different types of mixture mass flows.

Modeling debris flows as two interacting phases depends on the accuracy in which the physics controlling the constituents' motion are defined. The fluid phase is oftentimes a mixture of water and suspended fine particles. The work of Pudasaini (2012); Pudasaini and Mergili (2019), proposed a viscosity-dominated viscoplastic rheology model to simulate fluid dynamic behaviors. However, in cases where the solid fraction is low, the fluid phase can be modeled using a viscous-dominated rheology where the stresses are linearly related to the applied strain (Li and Zhao 2018; An et al. 2021). Previous debris flow simulations model the friction between the base and the flowing mass using the Coulomb and Voellmy friction models. Coulomb models consider the solid mass as a quasi-static block which moves once critical yield stress is exceeded and do not consider the frictional-collisional effects of particle contacts during shear. The Voellmy model is modified from the Coulomb model through the introduction of an additional term referred to as the turbulence coefficient (Voellmy 1955; Crosta et al. 2004). This coefficient however is empirical with no clear physical definition. Alternatively, the solid phase can be modeled as granular flows whereby frictional-collisional stresses experienced by the grains or particles control the motion and microstructure of the solid phase (Jop et al. 2006; Zhou et al. 2013). Recent research however has shown that in the presence of fluids, viscous stresses

and the energy dissipation that they induce should also be taken into consideration (Jop et al. 2006; Zhou et al. 2014; Amarsid et al. 2017; Cui et al. 2020).

In this work, the motion of a two-phase continuum is modeled using a hierarchical set of depth-averaged equations which incorporate a constitutive viscoinertial friction model that considers viscous effects on the solid phase. Here we aim to see whether the additional consideration of viscous stresses improve the ability to model debris flows relative to existing modelling frameworks which assume that only inertial stresses control the motion of the solid component in debris even when viscous interstitial fluids are present. The two-phase modelling framework is adopted from Pudasaini (2012) wherein interfacial interactions are modelled as buoyant, viscous drag, and virtual mass forces. Note that enhanced expressions for the viscous drag and virtual mass forces have been recently proposed in Pudasaini (2021) and Pudasaini (2019) respectively. However, in this work, the more generalized versions of these models are used instead. The applicability of the general modelling framework and the constitutive mode is tested against results obtained from instrumented flume experiments as well as on real documented debris flow events – the Yu Tung Road debris flow in Hong Kong. Modelling tests are also conducted on a debris flow case in the proximity of the Sichuan-Tibet Railway, which involves hazard risks to key man-made infrastructure.

2 Methodology

2.1 Depth-averaged Two-phase Model Derivation

In this study, following Pudasaini (2012); Bouchut et al. (2016), debris flows are modelled as solid-fluid mixtures flowing down slopes inclined at an angle θ_b . For convenience, we collectively denote the solid and fluid phases as $i = s, f$. In a coordinate system where the x-axis is along the flow direction, the y-axis points along the lateral direction, and the z-axis is perpendicular to the flow surface (see Fig. 1), the mass balance for each mixture phase i can be written as:

$$\frac{\partial \phi_i}{\partial t} + \nabla \cdot (\phi_i \vec{U}_i) = 0 \quad (1)$$

where $\bar{\mathbf{U}}_i = (u_i, v_i, w_i)$ is the velocity vector, and ϕ_i is the volume fraction.

The system can be treated as a shallow mass flow, i.e. the flow depth is much less than the length, whose dynamics can be expressed in terms of depth-averaged equations. We further assume that the surface tension is negligible; the solid and fluid components are incompressible; and no phase change occurs. Subject to the abovementioned simplifying assumptions, Equation (1) is depth-averaged and re-written as:

$$\frac{\partial h_i}{\partial t} + \frac{\partial(h_i u_i)}{\partial x} + \frac{\partial(h_i v_i)}{\partial y} = 0 \quad (2)$$

where h_i is the flow depth of the constituent phase. The depths of each flow phase represent their respective volumes within a unit computational cell and are related to the total flow height as $h_d = h_s + h_f$.

Following (Pudasaini 2012), the momentum balance equations for the solid and fluid phases can be written as:

$$\frac{\partial(\phi_i \rho_i \bar{\mathbf{U}}_i)}{\partial t} + \nabla \cdot (\phi_i \rho_i \bar{\mathbf{U}}_i \otimes \bar{\mathbf{U}}_i) = \phi_i \rho_i \bar{\mathbf{g}} - \nabla \cdot \phi_i \bar{\mathbf{T}}_i \pm \bar{\mathbf{F}}_i \quad (3)$$

where $\bar{\mathbf{g}}$ is the gravity vector, ρ_i is the material density and $\bar{\mathbf{T}}_i = (P_i \mathbf{1} + \boldsymbol{\tau}_i)$ is the stress tensor wherein P_i is the normal load (here referred to as the pressure), and $\boldsymbol{\tau}_i$ is the deviatoric component, and $\mathbf{1}$ is an identity matrix. In this work, we assume that the fluid stresses are controlled by a simple Newtonian rheology whereas the solid phase stresses are equivalent to those of granular flows which are controlled by the frictional-collisional interactions among particles (Baker et al. 2016). It is noted that in many cases, the fluid phase in debris flows are muddy slurries which are non-Newtonian fluids (Major and Pierson 1992; Pudasaini 2012). However, it will be shown in later chapters that a Newtonian fluid model is sufficient for the watery and highly-saturated debris flows considered here. In addition to these inertial stresses, the presence of viscous fluids also dampens particle motion whereby its characteristic time for shear-induced migration is altered (Cassar et al. 2005). The shear deformation of the granular component, expressed through $\boldsymbol{\tau}_i$, should therefore be expressed in such a way that it incorporates the energy dissipation resulting from both inertial and viscous stresses (Amarsid et al. 2017). This study accounts for these effects by adopting a visco-inertial constitutive rheology for the granular phase, the exact form of which is detailed in Section 2.2. This is a crucial deviation

from previous coupled two-phase models (Pudasaini 2012; Bouchut et al. 2016) which do not consider the fluid contribution to the micro-scale dynamics of the particle phase.

The final term on the right-hand side of equation (3) denotes the interfacial forces per unit volume exerted by the constituent phases on each other, i.e., \vec{F}_s is the force exerted by the fluid on the solid particles while \vec{F}_f is the force experienced by the fluid phase from the moving particles. The positive and negative signs denote the direction in which the interaction forces are acting on and ensure that there is no net interaction force on the whole granular-fluid mixture flow. These interaction forces are inherent to each phase and cancel out when added overall phases. In here, we set \vec{F}_s to be positive and \vec{F}_f to be negative. The exact forms of these interaction forces will be detailed in Section 2.3.

Adopting the same assumption as in Equation 2, and following Pudasaini (2012), the shallow mass flow momentum balance equations for both phases are derived for the x - and y -directions from Equations 3:

$$\frac{\partial h_i u_i}{\partial t} + \frac{\partial(h_i u_i^2 + \frac{1}{2} g_z h_i^2)}{\partial x} + \frac{\partial(h_i u_i v_i)}{\partial y} = g_x h_i - \tau_{ix} \pm \bar{F}_{ix} \quad (4)$$

$$\frac{\partial h_i v_i}{\partial t} + \frac{\partial(h_i u_i v_i)}{\partial x} + \frac{\partial(h_i v_i^2 + \frac{1}{2} g_z h_i^2)}{\partial y} = g_y h_i - \tau_{iy} \pm \bar{F}_{iy} \quad (5)$$

where \bar{F}_i is the depth-averaged interfacial force for $i = s, f$. The concentration of each phase is defined as $\phi_i = h_i / h_d$ wherein $\phi_s + \phi_f = 1$.

The above-written set of equations can be rearranged in a vector form as:

$$\partial_t V + \partial_x(H(V)) + \partial_y(G(V)) = S \quad (6)$$

where:

$$V = \begin{Bmatrix} h_i \\ h_i u_i \\ h_i v_i \end{Bmatrix}, \quad H(V) = \begin{Bmatrix} h_i u_i \\ h_i u_i^2 + \frac{g_z h_i^2}{2} \\ h_i u_i v_i \end{Bmatrix} \quad (7)$$

$$G(V) = \begin{Bmatrix} h_i v_i \\ h_i u_i v_i \\ h_i v_i^2 + g_z h_i^2 / 2 \end{Bmatrix}$$

$$S = \begin{Bmatrix} 0 \\ g_x h_i - \tau_{ix} \pm \bar{F}_{ix} \\ g_y h_i - \tau_{iy} \pm \bar{F}_{iy} \end{Bmatrix}$$

Current debris flow models also consider the erosion and entrainment of bed sediment (Iverson and Ouyang 2015; Zhang et al. 2019; Pudasaini and Krautblatter 2021; Guo et al. 2022). Flows that consider erosion can behave differently relative to those that do not. To isolate the influence of the granular friction model on the dynamics of debris flows, the effects of erosion and entrainment are not considered here. The physically correct and mathematically consistent, fully mechanical erosion-entrainment models and the mobility of the erosive mass flows are presented in Pudasaini and Krautblatter (2021).

2.2 Friction law for granular-fluid flows

In coupled two-phase flow models, stresses are defined separately for the solid and fluid constituent phases. Here we assume that the solid component behaves as dense granular flows saturated in fluid where the shear stress τ_s is a function of the flow effective friction and pressure, i.e. μP_s (Jop et al. 2006). In dry granular flows, the coefficient μ is controlled primarily by the frictional-collisional interactions of the particles (MiDi 2004) whereas in the presence of fluids, viscous forces exert an additional influence by hampering the motion of a moving particle by changing the characteristic time in which it undergoes shear-induced rearrangement (Du Pont et al. 2005; Cassar et al. 2005). Amarsid et al. (2017) proposed a constitutive rheological framework that captures the additive influence of inertial and viscous interactions in the form:

$$\mu(K) = \mu_c + \frac{\mu_d - \mu_c}{1 + K_0/K} \quad (8)$$

where μ_c and μ_d are critical friction coefficients defining the boundaries between which granular flows are considered to be dense, and are dependent on the particle material properties. It has been shown that these coefficients are also dependent on the particle size distribution (Staron and Phillips 2016; Cui et al. 2020) but

less so by the material properties of the interstitial fluid. The coefficient K_0 is a dimensionless constant that is specific to the system. The constant K is the so-called visco-inertial number which reflects the additive effects of the viscous and inertial stresses on the flow microstructure and frictional state:

$$K = \sqrt{I^2 + \varepsilon J} \quad (9)$$

where ε is a tuning parameter that measures the relative significance of viscous stresses in the system. The constants μ_c , μ_d , K_0 and ε are determined from data fitting of data obtained through experiments of steady granular flows (Forterre and Pouliquen 2003, 2008; Zhou et al. 2014) or from numerical simulations (Amarsid et al. 2017; Cui et al. 2020). The inertial component of the flow is controlled by the inertial number:

$$I = \frac{d_s \dot{\gamma}}{\sqrt{P_s / \rho_c}} \quad (10)$$

which is the ratio of the characteristic time for a particle with density ρ_s to freely fall a distance equal to the particle diameter d_s , under a confining P_s , over the flow shear rate $\dot{\gamma}$. In the presence of viscous interstitial fluids, particles reach a viscous limiting velocity after a characteristic time η_f / P_d (MiDi 2004; Cassar et al. 2005). In this regime, the flow dynamics is defined by:

$$J = \eta_f \dot{\gamma} / P_d \quad (11)$$

which is the so-called viscous number. The $\mu(K)$ rheology is developed to account for the contributions of inertial and viscous stresses on the motion of saturated granular flows. Although this constitutive model has only been validated using data from simulations (Amarsid et al. 2017; Cui et al. 2020), its derivation is based on observed physical phenomena. The visco-inertial number K is a function of the dimensionless inertial number I and viscous number J which are both well-known in granular physics and encode the shear rate-pressure dependence of particle motion in dense flows, although individually they only represent limiting cases where the interstitial fluid is negligible (MiDi 2004) and when it is relevant Boyer et al. (2011) respectively. (Cassar et al. 2005) demonstrates that when I and J are substituted into the $\mu(I)$ rheology (similar formulation as in equation (8)), data points from both dry and viscous granular flows (small particles

in water) collapse in a single scaling curve. It can be said that I controls the rheology of inertial flows where the influence of fluid is minimal, J defines particle motion in viscous fluids, whereas K controls the rheology of fluid-saturated granular flows falling within these limiting regimes. It is noted that other dry granular flows models, such as those by (Domnik et al. 2013), have been proposed wherein τ_s has additional linear dependence on the shear rate, whereas $\dot{\gamma}$ dependence in the visco-inertial rheology is exclusively through K . Through this they are able to capture the behavior of flows at very high shear while the $\mu(K)$ is limited by μ_d which limits its application to dense granular flows. The model of Domnik et al. (2013) also does not require any fitting coefficients. Nevertheless, this work is mostly interested with the evaluation of the impact of viscous stresses on the solid component of two-phase flows which is captured visco-inertial rheology.

In this study, we assume that the interstitial fluid is Newtonian where the stresses evolve linearly with the applied strain. The rheology of the fluid phase can be defined by the following constitutive law:

$$\tilde{T}_f = \eta_f [\nabla^T I_f + (\nabla \vec{U}_f)^T] \quad (12)$$

where $\nabla \vec{U}_f$ is the gradient of fluid velocity, and $(\cdot)^T$ is a transpose calculation operator. Integrating along the depth h_f , equation (12) can be written as:

$$\tilde{T}_f = \eta_f \frac{|\vec{U}_f|}{h_f} \quad (13)$$

2.3 Fluid-Solid interface interaction terms

The mixture phases are coupled by the forces that they exert on each other. The interaction between the fluid and the solid particles can be broken down into hydrostatic and hydrodynamic components. The hydrostatic force component accounts for the fluid pressure gradients around individual particles while hydrodynamic forces express the dependence on the relative motion between phases. In this work, interfacial interactions are modelled according to Pudasaini (2012) wherein the hydrostatic component is due to buoyancy f_b while the hydrodynamic component is from the drag f_d and virtual mass f_{VM} forces. The solid interfacial term \bar{F}_s is expressed as:

$$\bar{F}_s = f_b + f_d + f_{VM} \quad (14)$$

The fluid interfacial forces \bar{F}_f only include the hydrodynamic terms and are equal (but negative) to their solid counterparts. The buoyant force is formally written as:

$$f_b = P_f \nabla \phi_s \quad (15)$$

where P_f is the fluid pressure. The drag force accounts for the force acting opposite to the relative velocity between the solid material and surrounding fluid and is written as:

$$f_d = M_d h_d \quad (16)$$

where $M_d = C_d (\vec{U}_s - \vec{U}_f) |\vec{U}_s - \vec{U}_f|$ is the generalized momentum transfer term, and C_d is the drag force coefficient with the form (Pudasaini 2012):

$$C_d = \frac{\phi_s \phi_f (1 - \gamma)}{\left\{ \varepsilon U_T \left(P^* \Gamma(R_{ep}) + (1 - \gamma^*) \Omega(R_{ep}) \right) \right\}^2} \quad (17)$$

Note that in Pudasaini (2020), an additional damping term is introduced in the denominator to prevent singularities. Equation (17) is an idealized version of the drag coefficient wherein the damping coefficient is set to zero. The term $(\vec{U}_s - \vec{U}_f)$ is the relative velocity vector between phases, $\Gamma(R_{ep})$ and $\Omega(R_{ep})$ are the solid-like and fluid-like drag contributions that depend on particle-scale Reynold's number $R_{ep} = \frac{\rho_f d_s |\vec{U}_s - \vec{U}_f|}{\eta_f}$

and are formally expressed as:

$$\Gamma(R_{ep}) = \frac{\gamma R_{ep}}{180} \left(\frac{1 - \phi_s}{\phi_s} \right)^3 \quad (18)$$

$$\Omega(R_{ep}) = \varphi_f^{M(R_{ep})-1}, \quad (19)$$

where $\varepsilon = H/L$ and $\gamma = \rho_f / \rho_s$ are the aspect and the density ratios, respectively. The dimensionless parameter P^* serves combining the solid-like and fluid-like drag contribution of these two factors. The model has been extensively used and validated for a wide range of problems including debris flows, avalanches, and landslides (Kattel et al. 2016; Kattel et al. 2018; Kafle et al. 2019; Qiao et al. 2019; Mergili et al. 2020a; Mergili et al. 2020b; Shugar et al. 2021).

When a particle moves through a moving fluid body, the surrounding liquid is dragged by the particle to motion. This portion of the liquid mass attains the same velocity as the particle and results in a virtual increase in the particle mass which is translated as a force acting on the particle. This is referred to as the virtual mass force f_{VM} and is formally expressed as Pudasaini (2019):

$$f_{VM} = C_{VM} \frac{d}{dt} (\bar{\mathbf{U}}_s - \bar{\mathbf{U}}_f) \quad (20)$$

C_{VM} is virtual mass force coefficient which is equal to $\frac{(1+2\phi_s)}{2\phi_f}$. While In Pudasaini (2019), the virtual mass coefficient is extended to be smooth and well-bounded for mass flows within wider regime in the form of $\frac{N_{vm}-1}{\phi_s/\phi_f + \gamma}$ where the virtual mass number N_{vm} is the ratio of the relative velocities obtained from the virtual mass force enhanced relative mass fluxes and the relative velocities.

2.3 Computational implementation

The mathematical scheme used to numerically solve the abovementioned set of equations forms a crucial part in the effective modeling of debris flows. In this work, the standard Lax-Friedrich (LxF) central differencing scheme is adopted since it circumvents the Riemann characteristic decomposition while retaining high resolution (Zhou et al. 2020b). This scheme implements a piecewise-linear interpolation to achieve second-order resolution (Zhou et al. 2020b). A staggered grid is adopted to ensure numerical stability (Jiang et al. 1998; Jiang and Tadmor 1998). Staggering is necessary due to the fact that cell interfaces are stable in neighborhoods around smoothed regular mid-cells of the previous time step. The staggered form is then recast into a non-staggered form by re-averaging the reconstructed value of the staggered grid. This helps to overcome complexities near the boundaries, and the difficulties of values changing due to the alternate cells between time steps.

Based on the model definition in section 2.1, our numerical system can be summarized into Eqs. (6-7). After the equation is translated into depth-integrated form, the equations are discretized and solved using the central differencing scheme. Numerical time steps are set to be well below the Courant number to ensure numerical stability.

3 Model validation and simulation results

In this section we first calibrate the numerical model detailed in the previous section against results from instrumented flume experiments. Then a real debris flow case that occurred in Yu Tung Road, Hong Kong is used for testing our model.

3.1 Flume model tests

Figure 2a shows a schematic diagram of the instrumented flume used to conduct channelized granular-fluid flows and Figures 2b-c are the schematic diagrams showing the dimensions of the flume as viewed from the side and the top, respectively. The flume has an overall length of 10.2 m, a base width of 0.3 m, and a depth of 0.8 m. The flume is designed to have two segments having different inclinations – a steep upper channel L_1 (inclined at 25°) and a less inclined lower channel L_2 (inclined at 5°). Channel L_1 is 4.2 meters long and is intended to accelerate the flow while L_2 is 5.0 m in length and is designed to slow the flows down. The channel bed is made up of a steel plate which is roughened by gluing a layer of fine debris to its surface. Sidewalls are made up of transparent Perspex glass, which enables the observation of the dynamic process of the mixture flows. The particle-fluid mixture is released from a 1 m long rectangular storage tank with a total volume of 0.17 m³ when inclined at 25°.

Figures 2b illustrates the side view of the flume showing the positions of 5 ultrasonic distance sensors (USD), with resolutions of 0.1 cm, suspended over different sections of the flume and the load cells (LC) that are positioned directly below them. These two sensors, collectively referred to as a sensor unit (SU), measure the height and the basal normal stress of the flowing mixture. Figure 2c shows the positions of the 5 sensor units SU_1 – SU_5 from the top to the bottom of the flume.

The initial debris flow mass is assumed to have a constant solid concentration ϕ_s of 0.5. Glass beads, with diameters of 0.4-0.6 mm and a material density of 2750 kg/m³, represent the solid granular phase in debris flows. The viscous liquid used in the flume tests is a mixture of glycerol and water. Glycerol is adopted for its transparency, high solubility, and viscosity. The fluid density is 1200 kg/m³ with viscosity 0.05 Pa · s

(as measured from a torque rheometer). The solid and fluid mixture is uniformly mixed prior to its release down the flume.

The flume dimensions are replicated in the simulations. An end-wall boundary (b_w) for the flume sidewall is set to prevent outward flux, while an open boundary (b_o) is assigned at the end of flume which allows the material to exit the simulation domain. The simulation domain has a spatial resolution of $0.01\text{ m} \times 0.01\text{ m}$.

At $t = 0\text{ s}$, the mixture is homogeneous and is composed of 50 % solid and 50 % fluid, initiated in a rectangular reservoir ($800 \leq x \leq 1900\text{ mm}$; $400 \leq y \leq 700\text{ mm}$). Upon settling in the reservoir, a sluice gate located at $x = 1900\text{ mm}$ prevents the mixture from immediately flowing down the chute. The initial geometry of the simulated mixture, containing both solid and fluid phases, is defined by the following boundaries:

$$h_i = \begin{cases} 230\text{ mm} & \text{at } x = 1900\text{ mm} \\ (x - 800\text{ mm}) \sin 25^\circ & \text{if } 800\text{ mm} < x < 1900\text{ mm} \\ 0 & \text{otherwise} \end{cases}$$

Simulation parameters are kept consistent with experimental values and are summarized in Table 1. As a benchmark, frictional parameters (e.g. μ_c , μ_s , K_0) are obtained from values used in studies on the physics of two-phase subaerial and immersed granular mass flows (Pudasaini 2012; Cui et al. 2020).

When the gate is opened the mixture flows down the flume channel and the flow heights are recorded at the locations in which load cells and ultrasonic sensors are installed. Figure 3a shows that the incoming flows have bulbous flow heads, where the height is maximum and is thinner at the body. The flow height substantially decreases as it continues down the chute. Figure 3b shows the simulated flow heights from which a good agreement is found with the experimental measurements. It can be noticed, however, that the simulated flows are slower than the experimental flows especially at the low inclination segment of the flume (SU_3 to SU_5). This may partly be due to differences in the initial mixture conditions: in the simulations the solids and fluids are evenly mixed whereas inhomogeneities in the mixture concentration may exist in the experiments. This discrepancy may also be due to the drag and virtual mass forces used and could be improved using enhanced analytical models (Pudasaini 2019, 2020).

Figure 4a-c shows the distribution of the solid (red dashed lines) and fluid (blue dashed lines) flow heights at different points in time ($t=1,2,3$ s). At $t=1$ s (figure 4(a)), the fluid phase mostly gathers at the front while the solid phase accumulates at the middle of the flow body. As time progresses the solid components overtake the fluid and later on make up the bulk of the flow head leaving the tail to be highly fluidized. At the onset of flow, the fluid is more mobile and can easily slide faster downslope compared to the more frictional solid grains. Figure 4(d-f) compares the solid concentrations measured by SU_1-5 (blue symbols) with those obtained from the simulations (green line). Results from both experimental measurements and numerical simulations show a nearly pure solid head followed by a trailing fluid tail. As the mass flows downward, the body of the flow contains less solids at the center, while the front and tail are dominated by solid and fluid except for a short and nearly pure solid head. The solid volume concentration eventually evolves smoothly from the head to the tail along flow direction (Fig. 4e, f).

The phase separation of the solid and fluid observed here (as well as in the debris flow case documented in Section 3.2) is a common feature of two-phase flows and is captured by recent two-phase flow models (Pudasaini (2012) as well as in discrete-continuum numerical models (Leonardi et al. 2015). The work of Pudasaini and Krautblatter (2014) explains that the accumulation of the solid mass at the front is a consequence of the momentum exchange between the solid and fluid phases. The initial surge of fluid to the front results in mechanically weaker middle and back regions of the flow body but at the same time the greater momentum of the fluid in these regions pushes the solid mass towards the front. The particle matrix prevents the rapid flow of the fluid towards the front thereby resulting a solid dominated head. It is noted that a recent mechanical model by (Pudasaini and Fischer 2020) captures the evolution of particle rich heads and levees and fluid-like tail regions through the introduction of a phase separation flux mechanism in the governing equations. This separation flux is a function of the hydraulic pressure gradient, topography induced pressure gradients, the gradient of volume fraction, flow depths, and buoyancy (Pudasaini and Fischer 2020). Here, although we do not introduce the abovementioned flux term, phase separation still occurs. While particle rich levees are not observed possibly due to the confinement by the channel walls, the particle rich flow fronts emerge naturally. However, we could not identify the physical reason for the observed separation between

particles and fluid. Such phenomenon can only be physically described with the phase separation mechanics presented by Pudasaini and Fischer (2020).

3.2 Simulation of the Yu Tung Road debris flow

Extreme and prolonged rainfall triggered 19 landslides at the hillside area adjacent to the Yu Tung Road in Hong Kong. This quickly developed into a channelized debris flow that resulted to flooding and serious road blockage. In this study, we consider the largest channelized debris flow event that occurred in the said catchment. The Yu Tung debris flow is chosen as one of the test cases since it is a well-documented case of a saturated debris flow from which we can validate our proposed model against accurate field measurements.

Intense rainfall in the early morning of June 2008 resulted in a very channelized debris flow having an overall volume of $2,350 \text{ m}^3$ which travelled along the channel on the hillside above Yu Tung Road, Tung Chung, Northern Lantau district, Hong Kong. The maximum estimated velocity of the flow was nearly 12 m/s over a distance of 100 m from the source location which then decreased to about 10 m/s at 400 m. The total run-out distance is approximately 600 m. This debris flow was described to be very mobile due to having a highly fluidized head followed by a solids-rich flow body. After the event, the westbound lanes of Yu Tung Road were totally blocked and closed for over two month (Geotechnical Engineering Office 2012).

The study area is the hillside facing the northwest direction, 17 m to 27 m above the Yu Tung Road rising up to a maximum elevation of 482 m. The upper portion of the hillside is inclined at angles between 30° and 45° (Fig. 5), which include areas of large, exposed rocks. The hillside gradient in the mid-slope area is between 15° and 30° . The gradient decreases to less than 15° near the toe-slope area. The catchment can be divided into two segments: the transportation zone, and deposition zone. The mass can flow rapidly at the transportation zone then slow down and deposit at the deposition zone. The Yu Tung Road is at the toe-slope area with an elevation of around 30 m.

The hillside is densely covered with shrubs and bushes. Areas of colluvial boulder and rock exposure exist locally within the upper portion of the catchment. The site is underlain by metamorphosed rhyolite lava and tuff of the undivided Lantau Formation (Sewell and James 1985), later referred to as the Lantau Volcanic

Group, and locally mantled by debris flow deposits. Feldsparphyric rhyolite, banded lava, granite porphyry and tuff can be observed at the toe of the hillside (Sewell et al. 2000).

The debris flow event is simulated using the proposed two-phase model with the same frictional conditions used in the flume test. The simulation and material parameters used are summarized in Table 2. The solid volume concentration ϕ_s is set to be relatively low (0.3 – 0.5) implying that the mixture is highly saturated. Based on testimonies and video recordings of the event, the debris flow moved like a very rapid flood which appeared brown due to the entrained mud and soil particles. Initiation mechanisms are not modelled in this work and hence the mass is set to mobilize at t=0 s.

Figure 6a shows a comparison between the velocities obtained from the two-phase model simulations with velocity estimates of the actual event at certain points along the flow path labelled as A-E (green markers) for different solid concentrations $\phi_s = (0.3, 0.4, 0.5)$. Velocity profiles consistently show that the debris flow increases in velocity from initiation up until a distance of ~250 m where it reaches its peak velocity. Beyond this point, the flow slows down as it descends further until it reaches its deposition point at ~590 m. It is also observed that increasing ϕ_s slows down the flows, reflecting the enhanced flow mobility that results from the presence of interstitial fluids. Debris flows having $\phi_s = 0.4$ result in the best agreement with field observations.

Figure 6b shows predicted velocities from a typical single-phase flow model for the same range of ϕ_s . In contrast to two-phase models where stresses are defined separately for the solid and fluid constituents, the stresses of the mixture flow in single-phase models are defined by only one set of mass and momentum equations wherein calculated dynamic quantities are weighted by the phases' respective volume fractions. The single-phase model measurements do not agree well with field measurements and appear to be less sensitive with the changes in ϕ_s . This discrepancy is most evident in the data points beyond 400 m where the flow velocities are significantly underestimated. Figure 6c-f show the spatial evolution of flow velocity profiles at different calculation times.

Fig. 7 shows the solid fraction distribution for the times $t = 0, 16, 25, 33, 40$ s for two-phase flows with $\phi_s = 0.4$. The flow is initiated immediately at the start of the simulation and stress build-up due to the gradual

saturation associated with steady rainfall is neglected. After initiation, the flowing mass gains momentum as it moves downslope, then the flow runs into a steeper region which is near the catchment. At 16 s, it can be observed that most of the solids accumulate at the head followed by a fluid tail-region (Fig. 7b). At about 20 s, the flow runs into flatter terrain, in which the trailing fluids reach and overtake the solid phase. Some overflow is also observed since this portion of the catchment is shallow and is unable to confine the flow. Figure 7d shows that at $t = 33$ s, the main body of the debris flow continues to run along the catchment channel while leaving a trail of the material along the path. Portions of the flow are also observed outside the catchment channel. At round 40 s (Fig. 7e), the main body of the debris has stopped flowing and has totally blocked the Yu Tung Road while portions of the debris flow reach the other part of hill's side. The simulated deposition area and behavior is consistent with what is reported in the literature (Geotechnical Engineering Office 2012).

From Figure 7, it can be seen that the two-phase model captures the separation and relative motion of solid and fluid phases in the Yu Tung debris flow. To further investigate the driving factors that control the mobility of these phases we evaluate the forces that drive their motion. The driving forces are obtained from the right-hand side of the momentum balance in equations (4) and (5): the gravity term $G^* = gh \cos \theta_b$, basal friction term $F^* = \tau$, the viscous drag M_d^* , and the virtual mass force M_{VM}^* . These terms are normalized by u_i^2 and are plotted against time in Figure 8. The subscripts s and f denote the solid and fluid phases respectively. We evaluate these terms at two locations where one is at the narrow upper region P_1 (Fig. 8b), and the other is located at a flatter area P_2 (Fig. 8c) further downstream. Figure 8a shows the temporal evolution of ϕ_s at P_1 where it is observed that at the flow head is purely solid followed by a more fluidized body. The flow of phases in this region are both dominantly driven by the gravity G^* and is mainly opposed by the basal friction F^* . Correspondingly, Figure 8c shows that the fluid motion is also driven by gravity, especially at the rear of the flow where most of the fluid is situated, while the other forcing terms are negligible.

At P_2 where the terrain is less inclined, Figure 8d shows that the flow head is saturated, containing almost no solid components. Figure 8e shows that the solid phase motion is no longer gravity dominated and instead experiences greater basal friction which serves to oppose the motion of the flow. It is also observed that M_d^* is greater and positive in this region (relative to Figure 8a) which means that part of the solid motion is due to

the drag exerted by the fluid phase. The solid phase is subject to greater friction F_s^* than the fluid phase F_f^* which is probably why the latter is more mobile in this section and overtakes the solid phase at the flow head. Moreover, the basal friction of solid phase F_s^* is more sensitive to the variation of the basal angle as it is a function of the normal component of the gravitational acceleration g_z while F_f^* is not directly linked to the gravity component.

The phase separation that we observe in the simulations here result from the difference in the interactions of the solid and fluid phases with the terrain and from the momentum exchange of the phases with each other. Based on the analysis of momentum balance terms in Figure 8, the separation of the solid and fluid phases observed in the simulations result from their different interactions with the terrain and from the momentum exchange of the phases with each other. Phase separation however is a mechanical process which is accounted for in Pudasaini and Fischer (2020) using a separation flux mechanism that is dependent on the relative velocities of the solid and fluid phases resulting from the effective forces within the system. The separation flux is dependent on a separation rate, the solid and fluid volume fractions, and the flow height. Emergence of the separation fluxes in the mass balance equations result in the particle rich heads and levees and fluid-like tails in debris flows. As phase separation is dependent on the flow properties, it also has pronounced effects on the dynamics. As most of the particles accumulate to the front, the flow momentum and the impact potential increases (Iverson 1997). Particles at the levees keep the flow fluidized by preventing the fluid within the body to escape, thus promoting greater flow velocities and runoff distances. Accounting for phase separation in debris flow models is therefore vital for the design of resistive and mitigation structures (Pudasaini and Fischer 2020). It should be mentioned that the mixture of water and mud, as observed in the Yu Tung debris flow, may result in a complex non-Newtonian fluid. However, the results here show that modelling the liquid phase as a Newtonian fluid yields good simulations, probably due to the watery and highly saturated nature of the event. Although simplifications such as this may be useful for engineering purposes, physically relevant modelling should consider the non-Newtonian behavior of the fluid phase (Pudasaini and Mergili 2019).

4 Case study

In this section, our model is used to simulate real debris flow events which occurred in the Tianmo Gully near the Sichuan-Tibet Railway and national expressway G318.

4.1 Simulation of debris flows in the Sichuan-Tibet Railway area – the July 2018

Tianmo Gully debris flow

The Tianmo Gully is situated in Bomi County, Tibet, China which serves as a tributary to the Parlung Tsangpo River and It is located in the Parlung Tsangpo deep fault zone (Fig.9a). The drainage area is about 18 km², the main channel is 5 km long, and the average bed slope is $\sim 37^\circ$. The elevation of the mouth of Tianmo Gully is 2460 m a.s.l. and its highest peak is about 5560 m a.s.l. Modern glaciers in this region, covering an area of about 8 km², develop at elevations higher than 3800 m a.s.l., in the upper reaches of the valley (Yu et al. 2009; Ge et al. 2014; Deng et al. 2017; Qu et al. 2018). The gully basin is also rich in sediment, moraine soil deposits, and rock avalanche residuals that serve as loose solid materials for debris flows. Due to the steep terrain, abundant unconsolidated deposits, excessive rainfall, high temperature difference, and the accelerated glacial recession, debris flows are easily initiated in this area.

Several large-scale landslide events have been reported in this area. In 2007, heavy rainfall triggered the failure of glacial till-laden slopes in the upstream gully which resulted in serious damages to the national highway downstream (G318) including several casualties (Yu et al. 2009; Ge et al. 2014; Wei et al. 2018). In 2010, a debris flow was also triggered by heavy rainfall, blocked the Parlung Tsangpo river, and destroyed a bridge downstream. In 2018, saturation due to precipitation and glacier meltwater induced a massive debris flow at the right bank of the Tianmo gully with a total flowing volume of $1.8 \times 10^5 m^3$ (Gao et al. 2019). The debris flow rushed into Parlung Tsangpo River, temporarily blocking it and highway G318. The final debris flow deposition fan that formed on both banks of the river channel was 390 m long and 220 m wide (Gao et al. 2019). Figure 9b and c show snapshots of typical deposit profiles and lateral moraines in the Tianmo

Gully taken during a field investigation on April 2018, a few months before the debris flow event that is modelled here.

The debris flow event in 2018 is simulated as a two-phase flow wherein the solid phase is modelled using a viscoinelastic rheology with parameters similar to those used in the flume test and in the Yu Tung debris flow (refer to Table 2). The total volume of this event is $1.8 \times 10^5 m^3$ (Gao et al. 2019) and the source area is highlighted with a white line in Fig. 9a which is around 3 km from the downstream river. Fig. 10 shows the simulated height profiles for the times $t = 1, 90, 180 s$ for the two-phase flow model. The debris flow is initiated with a volume of $1.8 \times 10^5 m^3$ and is positioned at the right bank of the gully, located 2.6 km from the gully mouth. In here, the flow is initiated immediately at the start of the simulation and the mechanisms leading to the debris flow's initiation are ignored. After initiation, the flowing mass gains momentum and moves downslope, then the flow runs into a steeper region which is near the catchment. At about 90 s, the flow runs into flatter terrain which is near the mouth of Tiemo gully. At $t = 180 s$ (Fig. 10c), the main body of the debris has stopped flowing and has totally blocked the Parlung Tsangpo river while portions of the debris flow reach the other part of river bank. The debris flow has a maximum velocity of approximately 30 m/s. At the end of the flow, the maximum deposition height obtained at the middle of river bank is 9 m. This is comparable to the measurements of Gao et al. 2018 at the same location which is 8 m. Fig. 10c also shows that the simulated deposition area is consistent with what is reported (bounded by the red line) in the literature (Gao et al. 2019).

At this point, it is interesting to see whether adopting the $\mu(K)$ constitutive rheological model for the solid component, which accounts for the viscous dissipation experienced by the particles due to the presence of fluids (Jop et al. 2006; Zhou et al. 2014; Amarsid et al. 2017; Cui et al. 2020), improves the prediction of debris flows relative to other previously adopted models. Here, we compare simulations results using the $\mu(K)$, $\mu(I)$ (Jop et al. 2006; Zhou et al. 2013), and the classic Coulomb (Savage and Hutter 1989; Gray et al. 1999; Pudasaini and Hutter 2003; An et al. 2021) granular flow models. In classical Coulomb-type models the granular system moves only once it overcomes a critical yield stress and does not account for the changes in the effective friction resulting from the evolving flow dynamics. This model has been well studied and will

no longer be presented here. It is noted that in Pudasaini and Mergili (2019), Coulomb-type models are extended to evolve according to the flow dynamics, however this updated model is not considered here. The $\mu(I)$ constitutive model assumes that the fluidity of granular flows depends on the frictional-collisional interactions of the constituent particles. It is written similarly as equation (8), although substituting the dependence of the visco-inertial number K (equation 9) with I (equation 10). All of the three models depend on a critical friction μ_c which is a function of the particles' material friction angle. The $\mu(K)$ and $\mu(I)$ models both depend on additional parameters μ_d and K_0 (written as I_0 for the $\mu(I)$ model in the literature), which are made similar in order to facilitate comparison. Their respective values are summarized in Table 2.

Fig. 11a shows that flow velocities simulated by the Coulomb model tend to be much faster compared to the other two granular flow models which then may have contributed to the greater flow distances of the simulated flows. Figure 11b also shows that the simulated flow using the Coulomb model does not exhibit the bulbous deposit at the head and fails to capture the debris flows' blockage of the river channel, which is inconsistent with field observations. The results using the $\mu(I)$ and $\mu(K)$ rheology show comparable results and both models capture the blockage of the Parlun-Tsangpo river channel, although results obtained through the $\mu(I)$ model tend to be slightly greater. The near similarity is not unexpected since the $\mu(K)$ is basically an extended version of the $\mu(I)$. This also demonstrates that the flow is highly inertial and viscous influences are minimal. It can be also observed in Figure 11b that simulated deposit heights using the $\mu(K)$ show better agreement with the measurements of Gao et al. (2019) showing that incorporating the subtle influences of viscous stresses improves the modeling of granular-fluid phenomena such as debris flows. Results from simulations using a single-phase model, similar to those in Figure 6, are also shown (black dashed lines) for comparison. Flow velocities and final deposition heights obtained from the single-phase model are noticeably less than those obtained using two-phase models, regardless of the friction model used. This shows that a single-phase model is less sufficient in predicting the mobility of highly saturated debris flows and demonstrates that interfacial interactions and phase separation, which are unique features of two-phase flow models, are essential for the accurate prediction of the dynamic behaviors of debris flows. On the other hand, it can be observed in Figure 11b that simulation results of the deposit height using the $\mu(K)$ show better

agreement with the measurements of Gao et al. (2019) showing that incorporating the subtle influences of viscous stresses improves the modeling of granular-fluid phenomena such as debris flows. It should be noted that simulation results may be different when the non-Newtonian behavior of the fluid phase is considered or when interfacial interactions are considered differently (Pudasaini and Mergili 2019).

5 Conclusions and remarks

The motion of debris flows is controlled by the coupled dynamics of its solid and fluid constituents and can ideally be captured using a two-phase depth-averaged framework which simulates the motion and interaction of each phase. Solid and fluid interactions come in the form of buoyant, drag, and virtual mass forces. The solid phase is treated as a dense granular flow with the frictional resistance defined by the so-called visco-inertial $\mu(K)$ constitutive rheology which accounts for both the inertial and viscous stresses on the flow dynamics. The fluid phase is simply treated as a Newtonian slurry formed from the mixture of water and fine particles.

The two-phase model, which is based on Pudasaini (2012), is first tested and calibrated against results from instrumented flume experiments. The influence of interfacial interactions is evaluated from the flow height profiles and from the spatial-temporal evolution of the solid concentration. The model is then tested against observations and measurements of a highly saturated debris flow case in which the fluid effects to the mobility are relevant. Comparison with simulations conducted using a single-phase model reveals that a two-phase framework provides better predictions of the mobility of highly saturated debris flows showing that interfacial interactions and the rheology that results therein are necessary to accurately model debris flows. We further apply the model on the 2018 Tianmo gully debris flow, wherein the simulation shows good agreement with the literature. We also demonstrate that incorporating the effects of viscous stresses in the granular rheology improves the modeling of debris flows relative to other widely adopted granular flow models. The two-phase visco-inertial continuum model can be used to improve mitigation strategies for debris flows hazards in the areas surrounding the Sichuan Tibet Railway.

The model provides reasonable predictions of the deposition and dynamics but still suffers from several shortcomings. Among them is the assumption that the buoyancy only affects the effective weight of the solid phase despite the fact that pressure gradients may also exist along the lateral and streamwise directions. Here, we have also mostly considered cases where the solid phase is highly saturated. Difficulties arise when lower fluid volume fractions are used possibly since other interfacial forces, such as cohesion and matric suction (Zhou et al. 2018) are present and need additional consideration. In this study, we also mostly assume that the pore fluid is Newtonian although muddy slurries and mixtures of water and suspended fine particles may also exhibit non-Newtonian behaviors (Pudasaini 2012; Pudasaini and Merigli 2019). Although this simplification in the fluid phase allows us to adequately capture debris flow behaviors that are useful for engineering applications, the non-Newtonian behavior of the fluid has to be considered correctly in order to make the debris flow modelling physically meaningful. Similarly, although it is demonstrated here that debris flows can be adequately modelled using the $\mu(K)$ frictional model, it should be noted that this framework is originally derived for laboratory-scale granular flows and its applicability in more general settings and flow materials, and its validity against physical experiments need to be further investigated. For simplicity, granular phenomena such as particle size segregation (Cui et al. 2020; Zhou et al. 2020a), and phase separation (Pudasaini and Fischer 2020) that are relevant along the flow height and are also active processes during debris flow motion, are also neglected.

Acknowledgements

The authors acknowledge the financial support from the National Natural Science Foundation of China (Grant No. 41941017), the Key Collaborative Research Program of the Alliance of International Science Organizations (Grant No. ANSO-CR-KP-2021-07), the Chinese Academy of Sciences (CAS) "Light of West China" Program, and Sino-German Mobility Programme (Grant No. M-0145).

Reference

- Amarsid, L., Delenne, J.-Y., Mutabaruka, P., Monerie, Y., Perales, F., Radjai, F., 2017. Viscoinertial regime of immersed granular flows. *Physical Review E.* 96, 012901. <https://doi.org/10.1103/PhysRevE.96.012901>.
- An, H., Ouyang, C., Wang, D., 2021. A new two-phase flow model based on coupling of the depth-integrated continuum method and discrete element method. *Computers & Geosciences.* 146. <https://doi.org/10.1016/j.cageo.2020.104640>.
- Baker, J.L., Barker, T., Gray, J.M.N.T., 2016. A two-dimensional depth-averaged $\mu(I)$ -rheology for dense granular avalanches. *Journal of Fluid Mechanics.* 787, 367-395. <https://doi.org/10.1017/jfm.2015.684>.
- Bouchut, F., Fernández-Nieto, E.D., Mangeney, A., Narbona-Reina, C., 2016. A two-phase two-layer model for fluidized granular flows with dilatancy effects. *Journal of Fluid Mechanics.* 801, 166-221. <https://doi.org/10.1017/jfm.2016.417>.
- Boyer, F., Guazzelli, É., Pouliquen, O., 2011. Unifying Suspension and Granular Rheology. *Physical Review Letters.* 107, 188301. <https://doi.org/10.1103/PhysRevLett.107.188301>.
- Cassar, C., Nicolas, M., Pouliquen, O., 2005. Submarine granular flows down inclined planes. *Physics of Fluids.* 17, 103301. <https://doi.org/10.1063/1.2061874>.
- Crosta, G.B., Chen, H., Lee, C.F., 2004. Replay of the 1987 Val Pola Landslide, Italian Alps. *Geomorphology.* 60, 127-146. <https://doi.org/10.1016/j.geomorph.2003.07.015>.
- Cui, K.F.E., Zhou, G.G.D., Jing, L., Chen, Y., Song, D., 2020. Generalized friction and dilatancy laws for immersed granular flows consisting of large and small particles. *Physics of Fluids.* 32, 113312. <https://doi.org/10.1063/5.0024762>.
- De Haas, T., Braat, L., Leuven, J.R., Lohhorst, I.R., Kleinhans, M.G., 2015. Effects of debris flow composition on runout, depositional mechanisms, and deposit morphology in laboratory experiments. *Journal of Geophysical Research Earth Surface.* 120, 1949-1972. <https://doi.org/10.1002/2015JF003525>.
- Deng, M., Chen, N., Liu, M., 2017. Meteorological factors driving glacial till variation and the associated periglacial debris flows in Tianmo Valley, south-eastern Tibetan Plateau. *Natural Hazards and Earth System Sciences.* 17, 345-356. <https://doi.org/10.5194/nhess-17-345-2017>.
- Domnik, B., Pudasaini, S.P., Katzenbach, R., Miller, S.A., 2013. Coupling of full two-dimensional and depth-averaged models for granular flows. *Journal of Non-Newtonian Fluid Mechanics.* 201, 56-68. <https://doi.org/10.1016/j.jnnfm.2013.07.005>.
- Du Pont, S.C., Gondret, P., Perrin, B., Rabaud, M., 2003. Granular Avalanches in Fluids. *Physical Review Letters.* 90, 044301. <https://doi.org/10.1103/PhysRevLett.90.044301>.

- Fernández-Nieto, E.D., Bouchut, F., Bresch, D., Diaz, M.C., Mangeney, A., 2008. A new Savage-Hutter type model for submarine avalanches and generated tsunami. *Journal of Computational Physics.* 227, 7720-7754. <https://doi.org/10.1016/j.jcp.2008.04.039>.
- Forterre, Y., Pouliquen, O., 2003. Long-surface-wave instability in dense granular flows. *Journal of Fluid Mechanics.* 486, 21-50. <https://doi.org/10.1017/s0022112003004555>.
- Forterre, Y., Pouliquen, O., 2008. Flows of Dense Granular Media. *Annual Review of Fluid Mechanics.* 40, 1-24. <https://doi.org/10.1146/annurev.fluid.40.111406.102142>.
- Gao, B., Zhang, J., Wang, J., Chen, L., Yang, D., 2019. Formation mechanism and disaster characteristics of debris flow in the Tianmo gully in Tibet. *Hydrogeology & Engineering Geology.* 46. <https://doi.org/10.16030/j.cnki.issn.1000-3665.2019.05.19>.
- Ge, Y., Cui, P., Su, F., Zhang, J., Chen, X., 2014. Case history of the disastrous debris flows of Tianmo Watershed in Bomi County, Tibet, China: Some mitigation suggestions. *Journal of Mountain Science.* 11, 1253-1265. <https://doi.org/10.1007/s11629-014-2579-z>
- George, D.L., Iverson, R.M., 2014. A depth-averaged debris-flow model that includes the effects of evolving dilatancy. II. Numerical predictions and experimental tests. *Proceedings of the Royal Society A Mathematical, Physical & Engineering Sciences.* 470, 20130820. <https://doi.org/10.1098/rspa.2013.0820>.
- Geotechnical Engineering Office. 2012. Detailed Study Report Of The 7 June 2008 Landslides On The Hillside Above Yu Tung Road, Tung Chung
- Gray, J.M.N.T., Wieland, M., Hutter, K., 1999. Gravity-Driven Free Surface Flow of Granular Avalanches over Complex Basal Topography. *Proceedings of the Royal Society A: Mathematical, Physical and Engineering Sciences.* 455, 1841-1874. <https://doi.org/10.1098/rspa.1999.0383>.
- Guo, J., Cui, Y., Xu, W., Yin, Y., Li, Y., Jin, W., 2022. Numerical investigation of the landslide-debris flow transformation process considering topographic and entrainment effects: a case study. *Landslides.* 19, 773-788. [10.1007/s10346_021-01791-6](https://doi.org/10.1007/s10346_021-01791-6).
- Hungr, O., 1995. A model for the runout analysis of rapid flow slides, debris flows, and avalanches. *Canadian Geotechnical Journal.* 32, 610-623. <https://doi.org/10.1139/t95-063>.
- Iverson, R.M., 1997. The physics of debris flows. *Reviews of Geophysics.* 35, 245-296. <https://doi.org/10.1029/97rg00426>.
- Iverson, R.M., Denlinger, R.P., 2001. Flow of variably fluidized granular masses across three-dimensional terrain: 1. Coulomb mixture theory. *Journal of Geophysical Research: Solid Earth.* 106, 537-552. <https://doi.org/10.1029/2000jb900329>.

- Iverson, R.M., George, D.L., 2014. A depth-averaged debris-flow model that includes the effects of evolving dilatancy. I. Physical basis. *Proceedings of the Royal Society A: Mathematical, Physical and Engineering Sciences.* 470. <https://doi.org/10.1098/rspa.2013.0819>.
- Iverson, R.M., LaHusen, R.G., 1989. Dynamic pore-pressure fluctuations in rapidly shearing granular materials. *Science.* 246, 796-796. <https://doi.org/10.1126/science.246.4931.796>.
- Iverson, R.M., Ouyang, C., 2015. Entrainment of bed material by Earth-surface mass flows: Review and reformulation of depth-integrated theory. *Reviews of Geophysics.* 53, 27-58. <https://doi.org/10.1002/2013rg000447>.
- Jiang, G.-S., Levy, D., Lin, C.-T., Osher, S., Tadmor, E., 1998. High-Resolution Nonoscillatory Central Schemes With Nonstaggered Grids For Hyperbolic Conservation Laws. *Siam Journal on Numerical Analysis.* 35, 2147-2168. <https://doi.org/10.1137/S0036142997317560>.
- Jiang, G.-S., Tadmor, E., 1998. Nonoscillatory Central Schemes For Multidimensional Hyperbolic Conservation Laws. *SIAM Journal on Scientific Computing.* 19, 1892-1917. <https://doi.org/10.1137/S106482759631041X>.
- Jop, P., Forterre, Y., Pouliquen, O., 2006. A constitutive law for dense granular flows. *Nature.* 441, 727-730. <https://doi.org/10.1038/nature04801>.
- Kafle, J., Kattel, P., Mergili, M., Fischer, J.-T., Pudasaini, S.P., 2019. Dynamic response of submarine obstacles to two-phase landslide and tsunami impact on reservoirs. *Acta Mechanica.* 230, 3143–3169. <https://doi.org/10.1007/s00707-019-02457-0>.
- Kattel, P., Kafle, J., Fischer, J.-T., Mergili, M., Tuladhar, B.M., Pudasaini, S.P., 2018. Interaction of two-phase debris flow with obstacles. *Engineering Geology.* 242, 197-217. <https://doi.org/10.1016/j.enggeo.2018.05.023>.
- Kattel, P., Khattri, K.B., Pokhrel, P.R., Kafle, J., Tuladhar, B.M., Pudasaini, S.P., 2016. Simulating glacial lake outburst floods with a two-phase mass flow model. *Annals of Glaciology.* 57, 349-358. <https://doi.org/10.3189/2016AoG71A039>.
- Leonardi, A., Cabrera, M., Wittel, F.K., Kaitna, R., Mendoza, M., Wu, W., Herrmann, H.J., 2015. Granular front formation in free-surface flow of concentrated suspensions. *Physical Review E* 92, 052204. <https://doi.org/10.1103/PhysRevE.92.052204>.
- Li, X., Zhao, J., 2018. Dam-break of mixtures consisting of non-Newtonian liquids and granular particles. *Powder Technology.* 338, 493-505. <https://doi.org/10.1016/j.powtec.2018.07.021>.
- Liu, W., He, S., Li, X., Xu, Q., 2016. Two-dimensional landslide dynamic simulation based on a velocity-weakening friction law. *Landslides.* 13, 957-965. <https://doi.org/10.1007/s10346-015-0632-z>.
- Major, J.J., Pierson, T.C., 1992. Debris flow rheology: experimental analysis of fine-grained slurries. *Water Resources Research.* 28, 841–857. [https://doi.org/10.1016/0148-9062\(92\)92700-m](https://doi.org/10.1016/0148-9062(92)92700-m).

- Mergili, M., Jaboyedoff, M., Pullarello, J., Pudasaini, S.P., 2020a. Back calculation of the 2017 Piz Cengalo–Bondo landslide cascade with r.avaflow: what we can do and what we can learn. *Natural Hazards and Earth System Sciences*. 20, 505-520. <https://doi.org/10.5194/nhess-20-505-2020>.
- Mergili, M., Pudasaini, S.P., Emmer, A., Fischer, J.-T., Cochachin, A., Frey, H., 2020b. Reconstruction of the 1941 GLOF process chain at Lake Palcacocha (Cordillera Blanca, Peru). *Hydrology and Earth System Sciences*. 24, 93-114. <https://doi.org/10.5194/hess-24-93-2020>.
- MiDi, G., 2004. On dense granular flows. *European Physical Journal E*. 14, 341–365. <https://doi.org/10.1140/epje/i2003-10153-0>.
- Ouyang, C., He, S., Tang, C., 2015. Numerical analysis of dynamics of debris flow over erodible beds in Wenchuan earthquake-induced area. *Engineering Geology*. 194, 62-72. <https://doi.org/10.1016/j.enggeo.2014.07.012>.
- Patra, A.K., Bauer, A.C., Nichita, C., Pitman, E.B., Sheridan, M.F., Bursik, M., Rupp, B., Webber, A., Stinton, A., Namikawa, L., 2005. Parallel adaptive numerical simulation of dry avalanches over natural terrain. *Journal of Volcanology and Geothermal Research*. 139, 1-21. <https://doi.org/10.1016/j.jvolgeores.2004.06.014>.
- Pitman, E.B., Le, L., 2005. A two-fluid model for avalanche and debris flows. *Philosophical Transactions of the Royal Society A: Mathematical, Physical and Engineering Sciences*. 363, 1573-1601. <https://doi.org/10.1098/rsta.2005.1596>.
- Pudasaini, S.P., 2012. A general two-phase debris flow model. *Journal of Geophysical Research: Earth Surface*. 117. <https://doi.org/10.1029/2011jf002186>.
- Pudasaini, S.P., 2019. A fully analytical model for virtual mass force in mixture flows. *International Journal of Multiphase Flow*. 113, 142-152. <https://doi.org/10.1016/j.ijmultiphaseflow.2019.01.005>.
- Pudasaini, S.P., 2020. A full description of generalized drag in mixture mass flows. *Engineering Geology*. 265, 105429. <https://doi.org/10.1016/j.enggeo.2019.105429>.
- Pudasaini, S.P., Fischer, J.-T., 2020. A mechanical model for phase separation in debris flow. *International Journal of Multiphase Flow*. 129. <https://doi.org/10.1016/j.ijmultiphaseflow.2020.103292>.
- Pudasaini, S.P., Hutter, K., 2003. Rapid shear flows of dry granular masses down curved and twisted channels. *Journal of Fluid Mechanics*. 495, 193-208. <https://doi.org/10.1017/s0022112003006141>.
- Pudasaini, S.P., Krautblatter, M., 2014. A two-phase mechanical model for rock-ice avalanches. *Journal of Geophysical Research: Earth Surface*. 119, 2272-2290. <https://doi.org/10.1002/2014jf003183>.
- Pudasaini, S.P., Krautblatter, M., 2021. The Mechanics of Landslide Mobility with Erosion. *Nature Communications*. 12, 1-15. <https://doi.org/10.1038/s41467-021-26959-5>.
- Pudasaini, S.P., Mergili, M., 2019. A Multi-Phase Mass Flow Model. *Journal of Geophysical Research: Earth Surface*. 124, 2920-2942. <https://doi.org/10.1029/2019JF005204>.

- Pudasaini, S.P., Wang, Y., Hutter, K., 2005. Modelling debris flows down general channels. *Natural Hazards and Earth System Sciences*. 5, 799-819. <https://doi.org/10.5194/nhess-5-799-2005>.
- Qiao, C., Ou, G., Pan, H., 2019. Numerical modelling of the long runout character of 2015 Shenzhen landslide with a general two-phase mass flow model. *Bulletin of Engineering Geology and the Environment*. 78, 3281-3294. <https://doi.org/10.1007/s10064-018-1329-z>.
- Qu, Y., Xiao, J., Pan, Y., 2018. Preliminary analysis on formation conditions of glacier debris flow in Southeast Tibet —a case of glacial debris flow in Tianmo Gully. *Water Resources and Hydropower Engineering*. 49, 177-184. <https://doi.org/10.13928/j.cnki.wrahe.2018.12.024>.
- Savage, S.B., Hutter, K., 1989. The motion of a finite mass of granular material down a rough incline. *Journal of Fluid Mechanics*. 199, 177-215. <https://doi.org/10.1017/S0022112089000340>.
- Sewell, R.J., Campbell, S., Fletcher, C., Lai, K.W., Kirk, P.A., 2000. *The PreQuaternary Geology of Hong Kong*. The PreQuaternary Geology of Hong Kong
- Sewell, R.J., James, J., 1985. Geology of North Lantau Island and Ma Wan. *Geology of North Lantau Island and Ma Wan*
- Shugar, D.H., Jacquemart, M., Shean, D., Bhushan, S., Upadhyay, K., Sattar, A., Schwanghart, W., McBride, S., de Vries, M.V.W., Mergili, M., Emmer, A., Deschamps-Berger, C., McDonnell, M., Bhambri, R., Allen, S., Berthier, E., Carrivick, J.L., Clague, J.J., Dokukin, M., Dunning, S.A., Frey, H., Gascoin, S., Haritashya, U.K., Huggel, C., Kaab, A., Kargel, J.S., Kavanaugh, J.L., Lacroix, P., Petley, D., Rupper, S., Azam, M.F., Cook, S.J., Dimri, A.P., Eriksson, M., Farinotti, D., Fiddes, J., Gnyawali, K.R., Harrison, S., Jha, M., Koppe, M., Kumar, A., Leinss, S., Majeed, U., Mal, S., Muhuri, A., Noetzli, J., Paul, F., Rashid, I., Scanin, Y., Steiner, J., Ugalde, F., Watson, C.S., Westoby, M.J., 2021. A massive rock and ice avalanche caused the 2021 disaster at Chamoli, Indian Himalaya. *Science*. 373, 300-306. <https://doi.org/10.1126/science.abh4455>.
- Staron, L., Phillips, J.C., 2016. How large grains increase bulk friction in bi-disperse granular chute flows. *Computational Particle Mechanics*. 3, 367-372. <https://doi.org/10.1007/s40571-015-0068-1>.
- Voellmy, A., 1955. ber die Zerstörungskraft von Lawinen.
- Wei, R., Zeng, Q., Davies, T., Yuan, G., Wang, K., Xue, X., Yin, Q., 2018. Geohazard cascade and mechanism of large debris flows in Tianmo gully, SE Tibetan Plateau and implications to hazard monitoring. *Engineering Geology*. 233, 172-182. <https://doi.org/10.1016/j.enggeo.2017.12.013>.
- Yu, Z., De, Q., Zhuo, g., ren, L.b.C., Deng, R., 2009. Preliminary analysis about the cause of “9.4” debris flow disaster in Tian mo gou, Bomi, Tibet. <https://doi.org/10.16031/j.cnki>.
- Zhang, L., Xiao, T., He, J., Chen, C., 2019. Erosion-based analysis of breaching of Baige landslide dams on the Jinsha River, China, in 2018. *Landslides*. 16, 1965-1979. <https://doi.org/10.1007/s10346-019-01247-y>.

- Zhou, G.G., Ng, C.W., Sun, Q.C., 2014. A new theoretical method for analyzing confined dry granular flows. *Landslides.* 11, 369-384. <https://doi.org/10.1007/s10346-013-0397-1>.
- Zhou, G.G.D., Cui, K.F.E., Jing, L., Zhao, T., Song, D., Huang, Y., 2020a. Particle Size Segregation in Granular Mass Flows With Different Ambient Fluids. *Journal of Geophysical Research: Solid Earth.* 125. <https://doi.org/10.1029/2020jb019536>.
- Zhou, G.G.D., Roque, P.J.C., Xie, Y., Song, D., Chen, H., 2020b. Numerical study on the evolution process of a geohazards chain resulting from the Yigong landslide. *Landslides.* 17, 2563-2576. <https://doi.org/10.1007/s10346-020-01448-w>.
- Zhou, G.G.D., Song, D., Choi, C.E., Pasuto, A., Sun, Q.C., Dai, D.F., 2018. Surge impact behavior of granular flows: effects of water content. *Landslides.* 15, 695–709. <https://doi.org/10.1007/s10346-017-0908-6>.

Table 1 Parameters used in flume simulations

Scope	Parameter	Definition	Value
Flume dimensions	V_{max}	Maximum capacity(m^3)	0.17
	V	Volume adopted in this study (m^3)	0.08
	θ_1, L_1	Acceleration section slope ($^\circ$) and length (m)	25, 4.2
	θ_2, L_2	Deceleration section slope ($^\circ$) and length (m)	5, 6.0
	w, d	Flume width (m) and depth (m)	0.3, 0.8
Solid phase	μ_c	Lower bound of dense granular flow	0.38
	μ_d	Upper bound of dense granular flow	0.64
	K_0	Dimensionless constant	0.28
	ρ_s	Particle density (kg/m^3)	2750
Fluid phase	ρ_f	Fluid density (kg/m^3)	1200
	η_f	Viscosity of fluid phase ($Pa \cdot s$)	0.05

	Parameter	Definition	Value
Event	V	The total volume (m^3)	2350
	R	Map spatial resolution (m)	2
	θ	Maximum inclination ($^\circ$)	45
	L	Runout distance (m)	600
Solid phase	μ_c	Lower bound of dense granular flow	0.38
	μ_d	Upper bound of dense granular flow	0.64
	K_0	Dimensionless constant	0.28
	ρ_s	Particle density (kg/m^3)	2750
Fluid phase	ρ_F	Fluid density (kg/m^3)	1200
	n	Manning coefficient	0.025
	η_F	Viscosity of fluid phase	0.05

List of figures

Fig. 1. Schematic diagram of a gravity-driven granular-fluid flow down a rough incline.

Fig. 2. (a) Schematic diagram of the experimental flume. The (b) side-view and (c) plan view of the model flume showing its dimensions and the positions of the ultrasonic distance sensors (USD) and load cells (LC) which make up a sensor unit. The values indicated in the diagrams are expressed in millimeters.

Fig. 3. (a) Measured and (b) calculated flow heights at different locations along the flume.

Fig. 4. (a-c) The total mass flow height (green lines) including those of the solid (red lines) and fluid phases (blue lines) along streamwise direction at $t = 1, 2, 3$ s. (d-f) The corresponding solid volume concentration ϕ_s along longitudinal distance. The green markers represent the predicted values while the blue markers are measurements from the experimental tests.

Fig. 5. (a) A side view photo of the channelized debris flow catchment adjacent to Yu Tung Road, Lantau Hillside, Hong Kong, the demarcations across the debris flow channel indicate the locations where flow velocities are measured. (b) The topography of the Yu Tung debris flow catchment.

Fig. 6. (a) Calculated velocity profiles from the two-phase model for $\phi_s = (0.3, 0.4, 0.5)$, (b) velocity profiles from the single-phase model for ϕ_s with the same values. The green points in (a-b) are the known velocities in certain regions by field measurement, (c-f) the contour maps from best-fit velocities result of multi-phase model ($\phi_s = 0.4$) at different calculation times $t = 0, 10, 30, 40$ s, respectively.

Fig. 7. (a-e) The distribution of the solid fraction for $\phi_s = 0.4$ at different calculation times ($t=0, 16, 25, 33, 40$ s).

Fig. 8. (a-b) The distribution of solid volume fractions with time at P_1, P_2 and the influence of the driving forces on their evolution at measurement points (b-c) P_1 and (e-f) P_2 .

Fig. 9. (a) High-resolution satellite image of the Tianmo Gully, (b) the deposit profiles at the glacier tongue area, (c) the deposit profile of the lateral moraine

Fig. 10. (a-c) The total flow height profiles at time $t = 1, 90, 180$ s respectively.

Fig. 11. (a-b) Velocity and height simulation profiles using different typical solid phase constitutive laws.

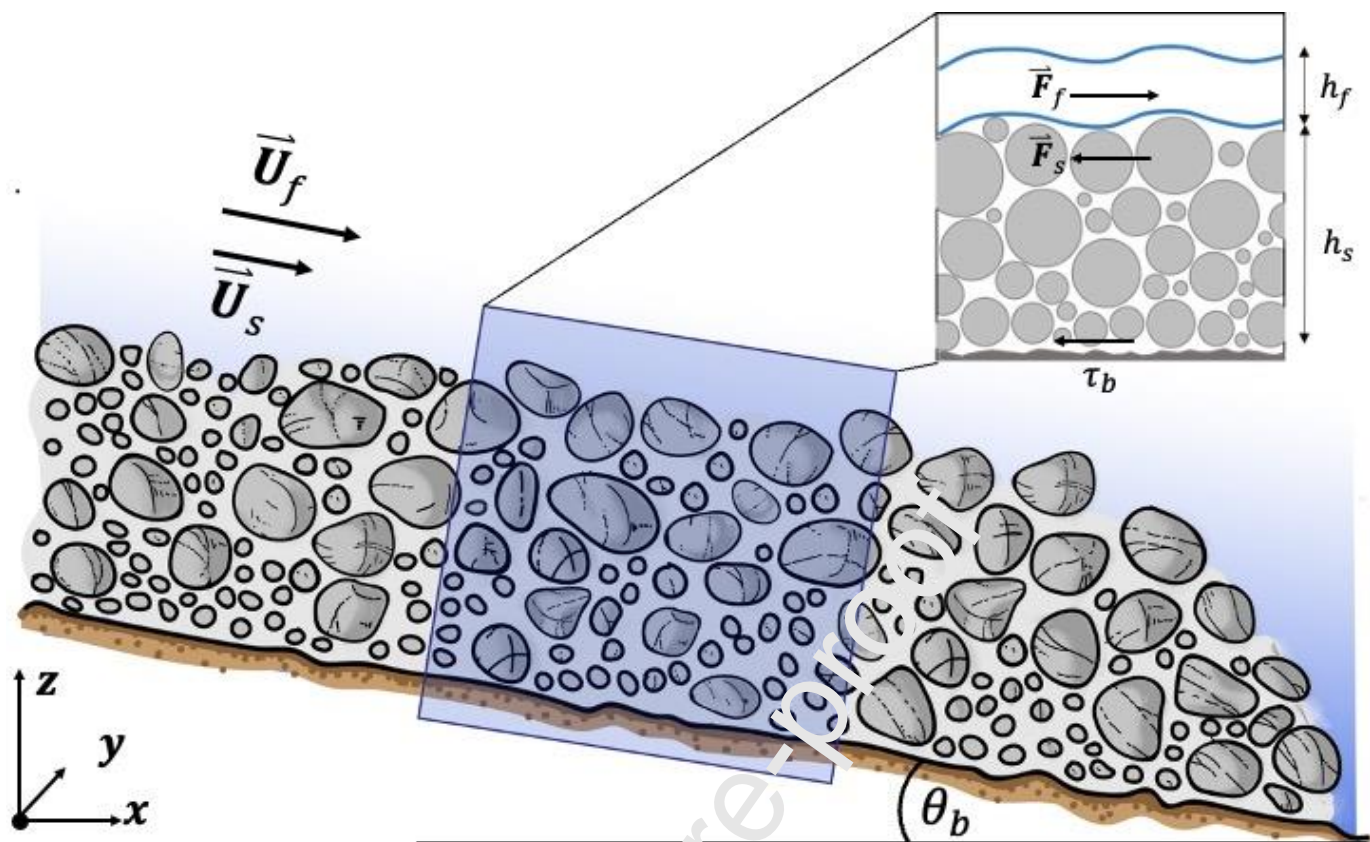


Fig. 1. Schematic diagram of a gravity-driven granular-fluid flow down a rough incline.

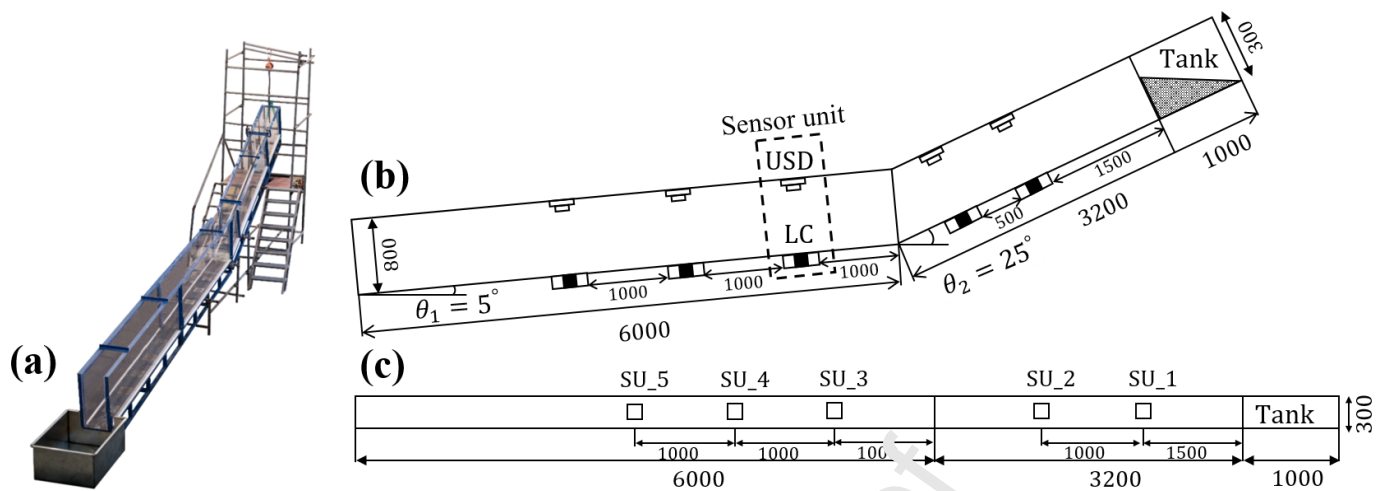


Fig. 2. (a) Schematic diagram of the experimental flume. The (b) side view and (c) plan view of the model flume showing its dimensions and the positions of the ultrasonic distance sensors (USD) and load cells (LC) which make up a sensor unit. The values indicated in the diagrams are expressed in millimeter

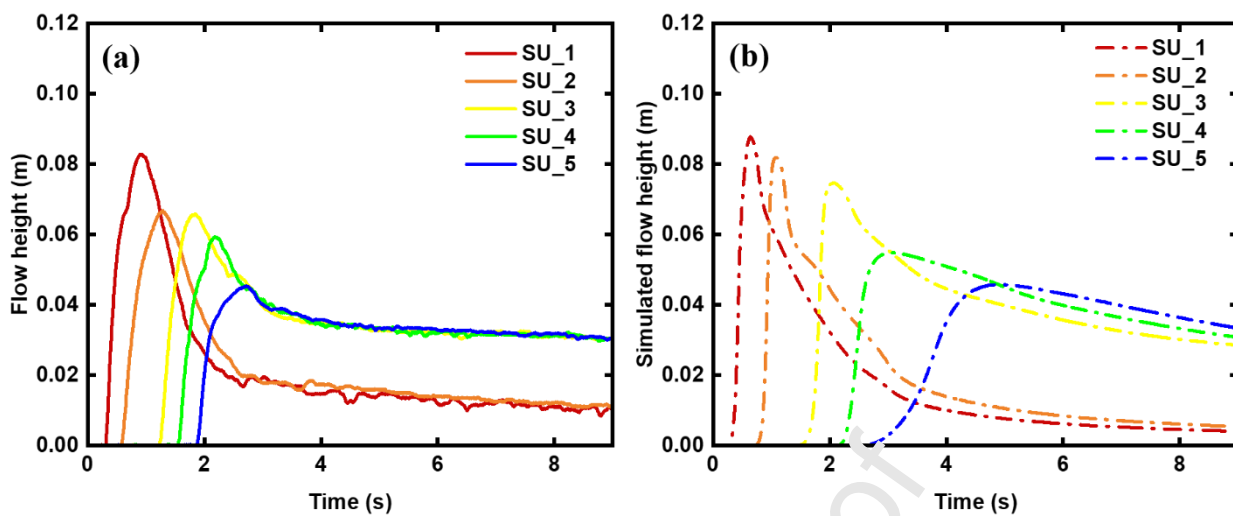


Fig. 3. (a) Measured and (b) calculated flow heights at different locations along the flume.

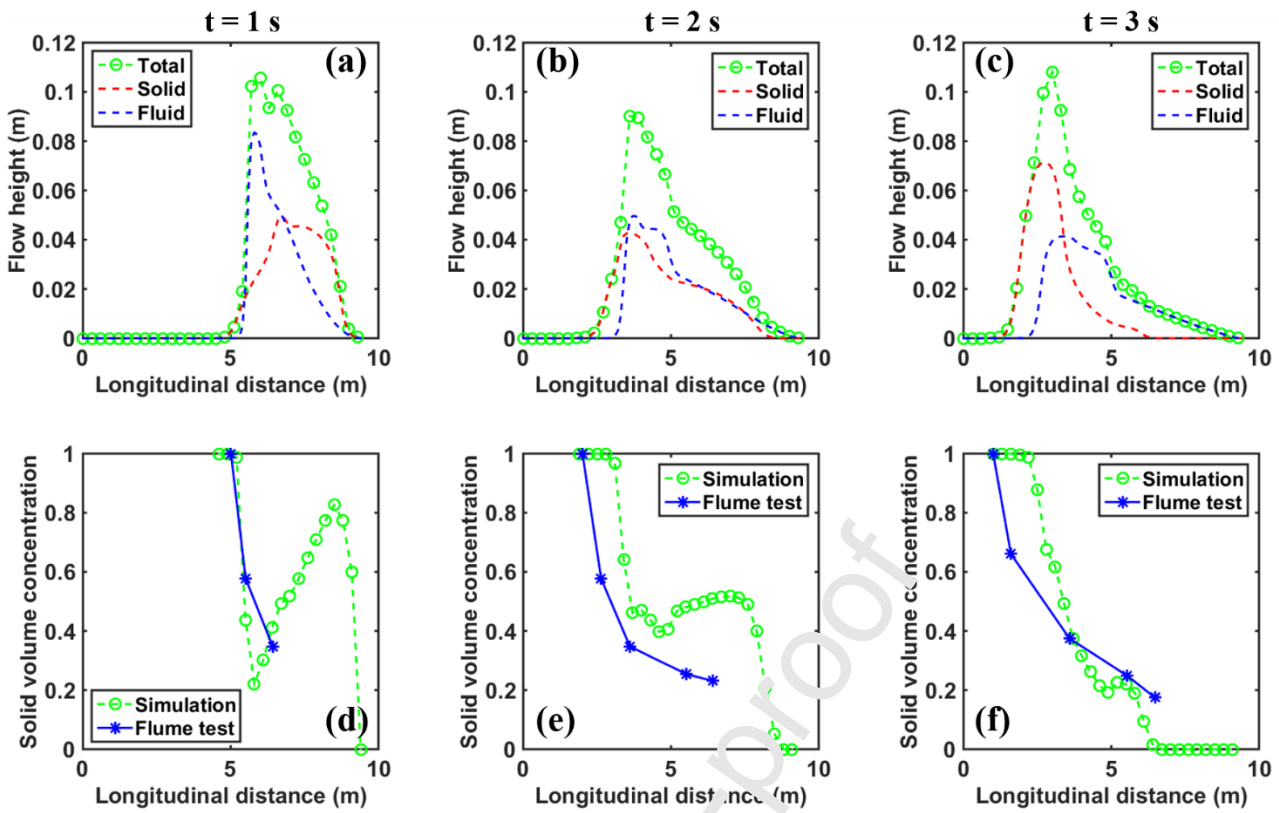


Fig. 4. (a-c) The total mass flow height (green lines) including those of the solid (red lines) and fluid phases (blue lines) along streamwise direction at $t = 1, 2, 3\text{ s}$. (d-f) The corresponding solid volume concentration ϕ_s along longitudinal distance. The green markers represent the predicted values while the blue markers are measurements from the experimental tests.

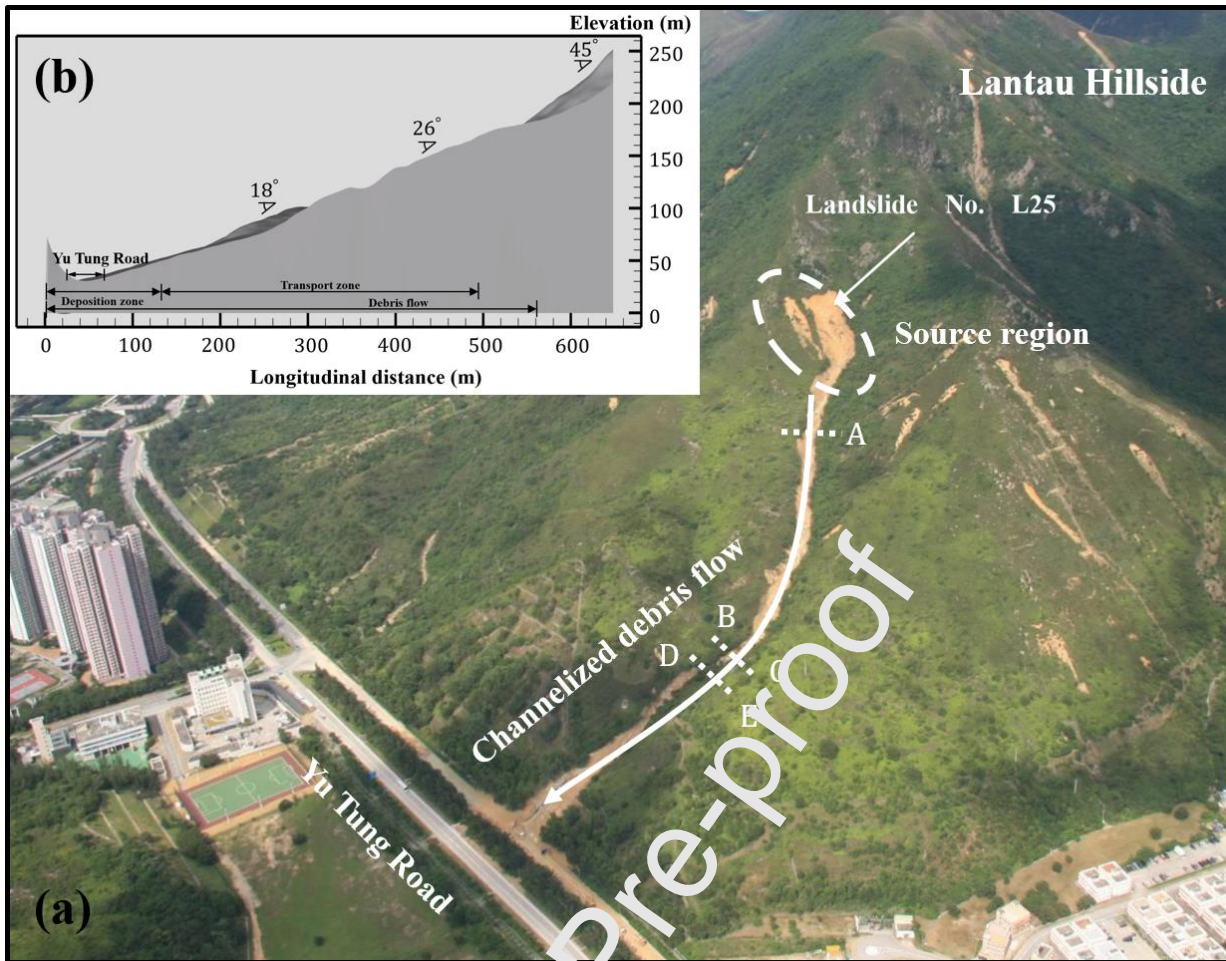


Fig. 5. (a) A side view photo of the channelized debris flow catchment adjacent to Yu Tung Road, Lantau Hillside, Hong Kong, the demarcations across the debris flow channel indicate the locations where flow velocities are measured. (b) The topography of the Yu Tung debris flow catchment.

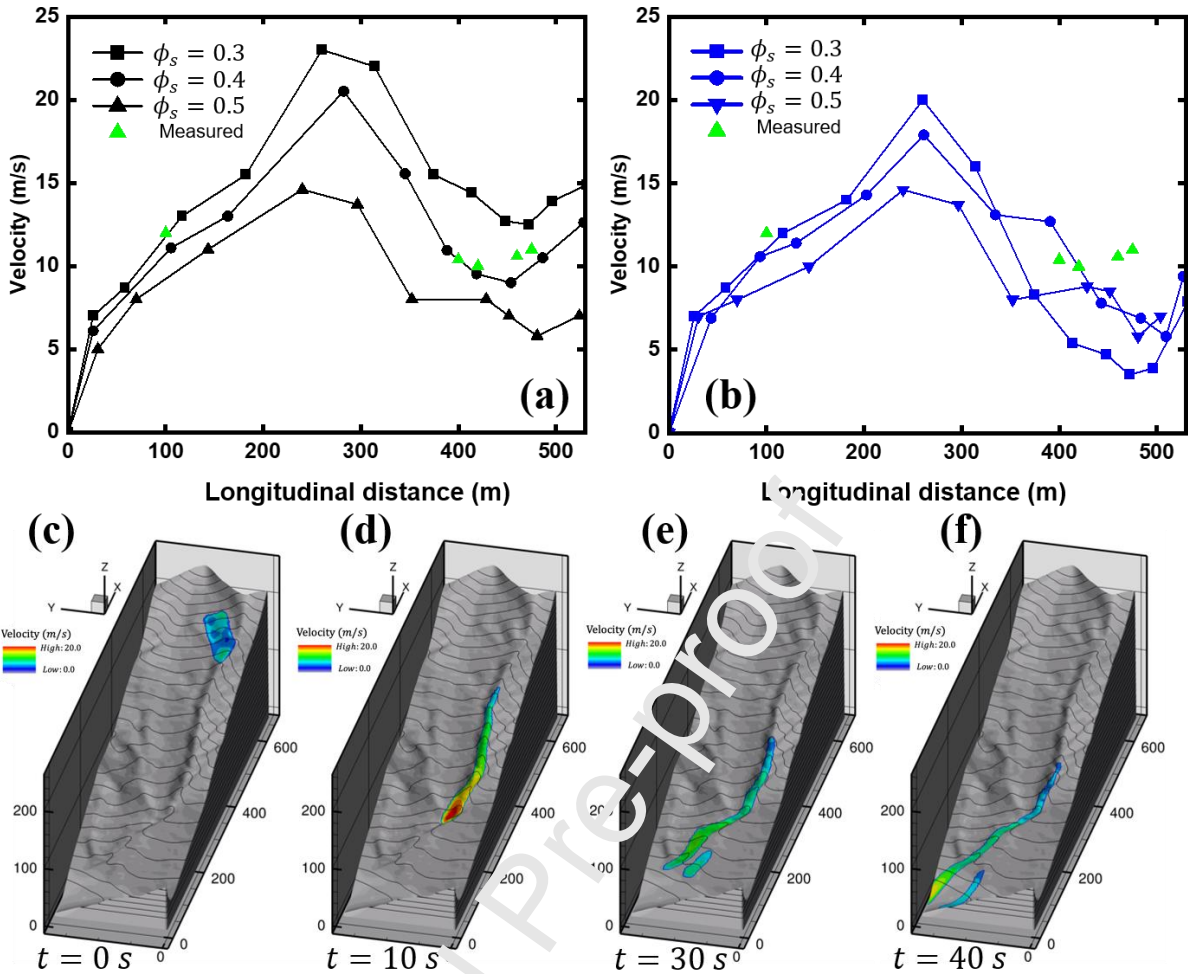


Fig. 6. (a) Calculated velocity profiles from the two-phase model for $\phi_s = (0.3, 0.4, 0.5)$, (b) velocity profiles from the single-phase model for ϕ_s with the same values. The green points in (a-b) are the known velocities in certain regions by field measurement, (c-f) the contour maps from best-fit velocities result of multi-phase model ($\phi_s = 0.4$) at different calculation time $t = 0, 10, 30, 40\text{ s}$, respectively.

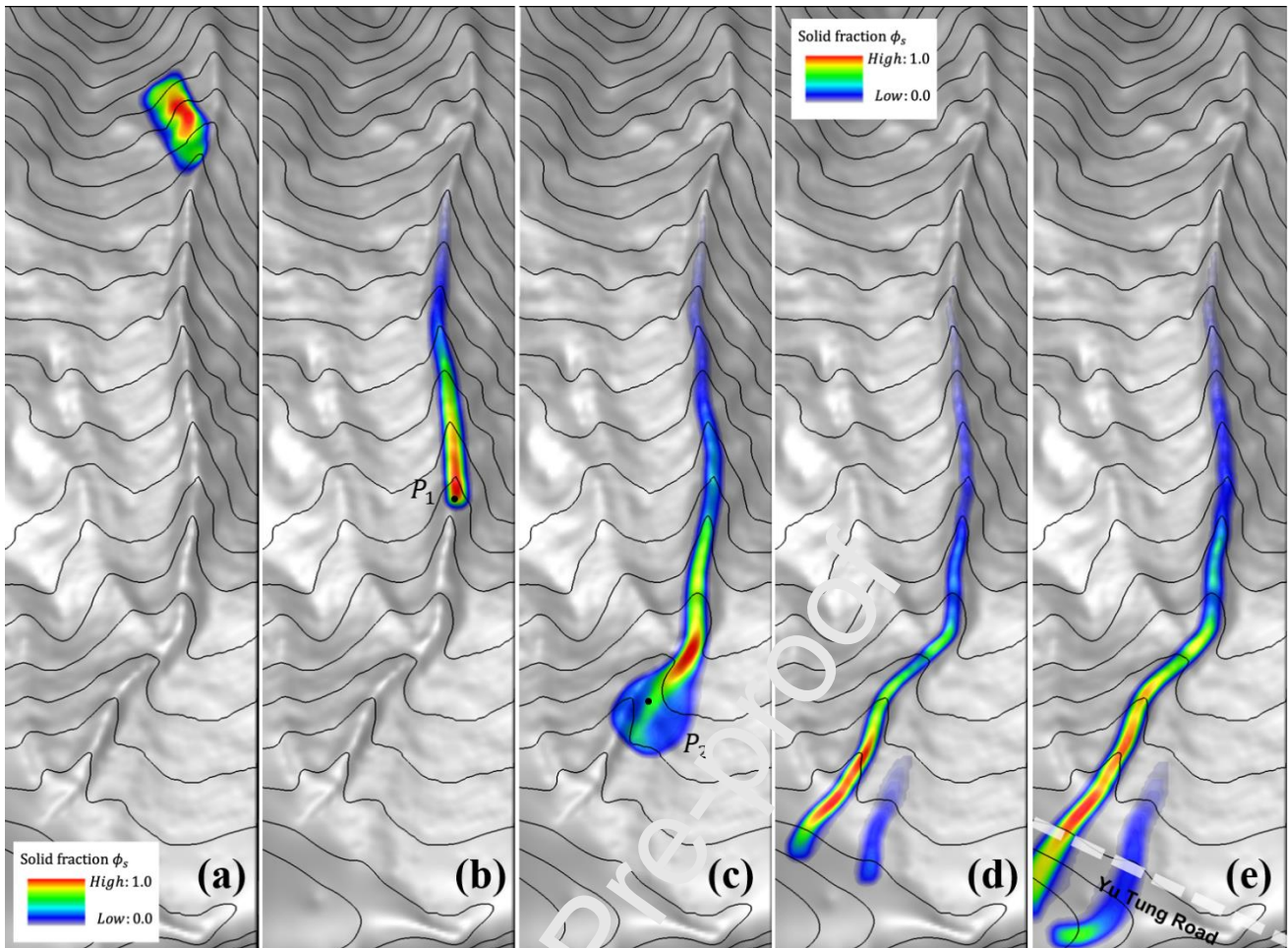


Fig. 7. (a-e) The distribution of the solid fraction for $\phi_s = 0.4$ at different calculation times ($t=0, 16, 25, 33, 40$ s).

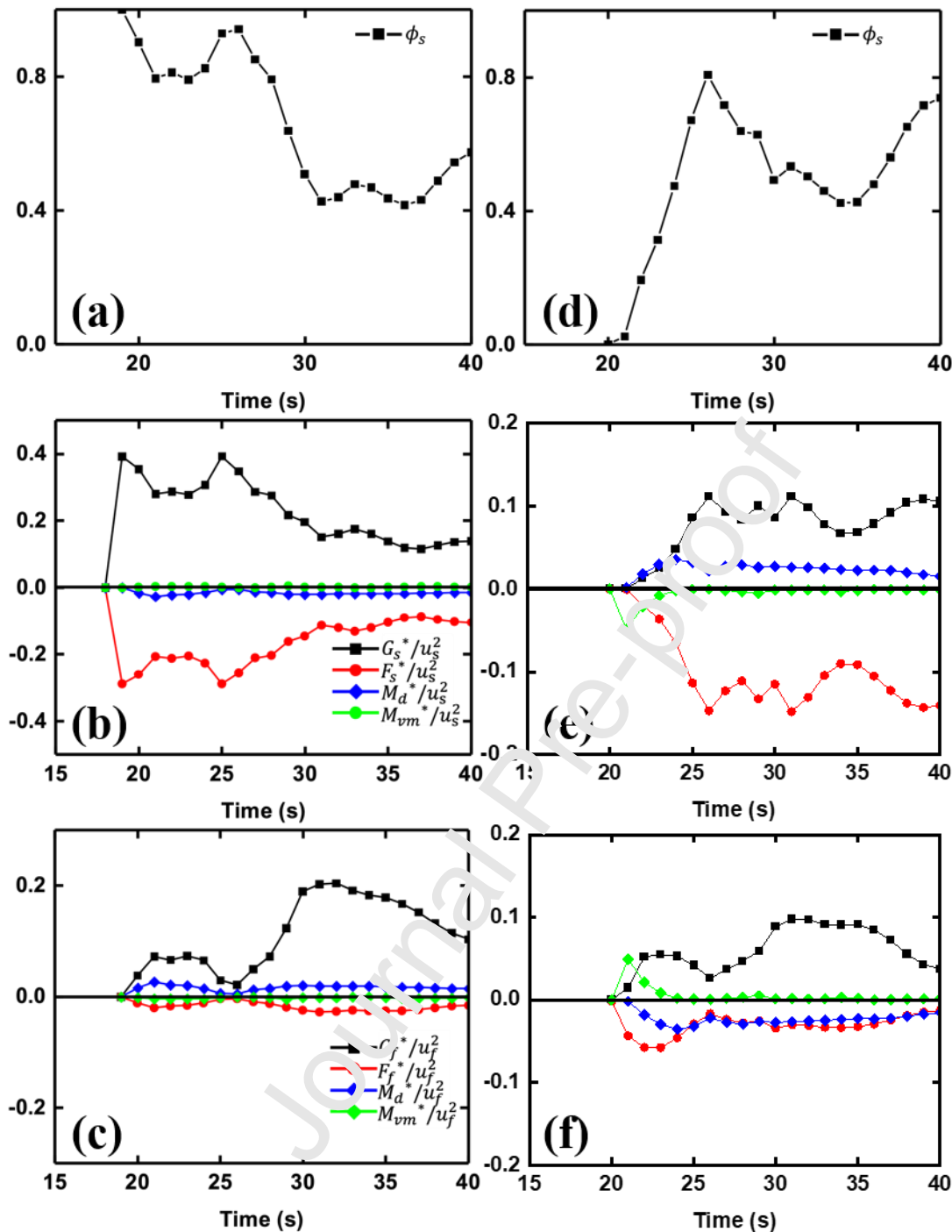


Fig. 8. (a-b) The distribution of solid volume fractions with time at P_1, P_2 and the influence of the driving forces on their evolution at measurement points (b-c) P_1 and (e-f) P_2 .

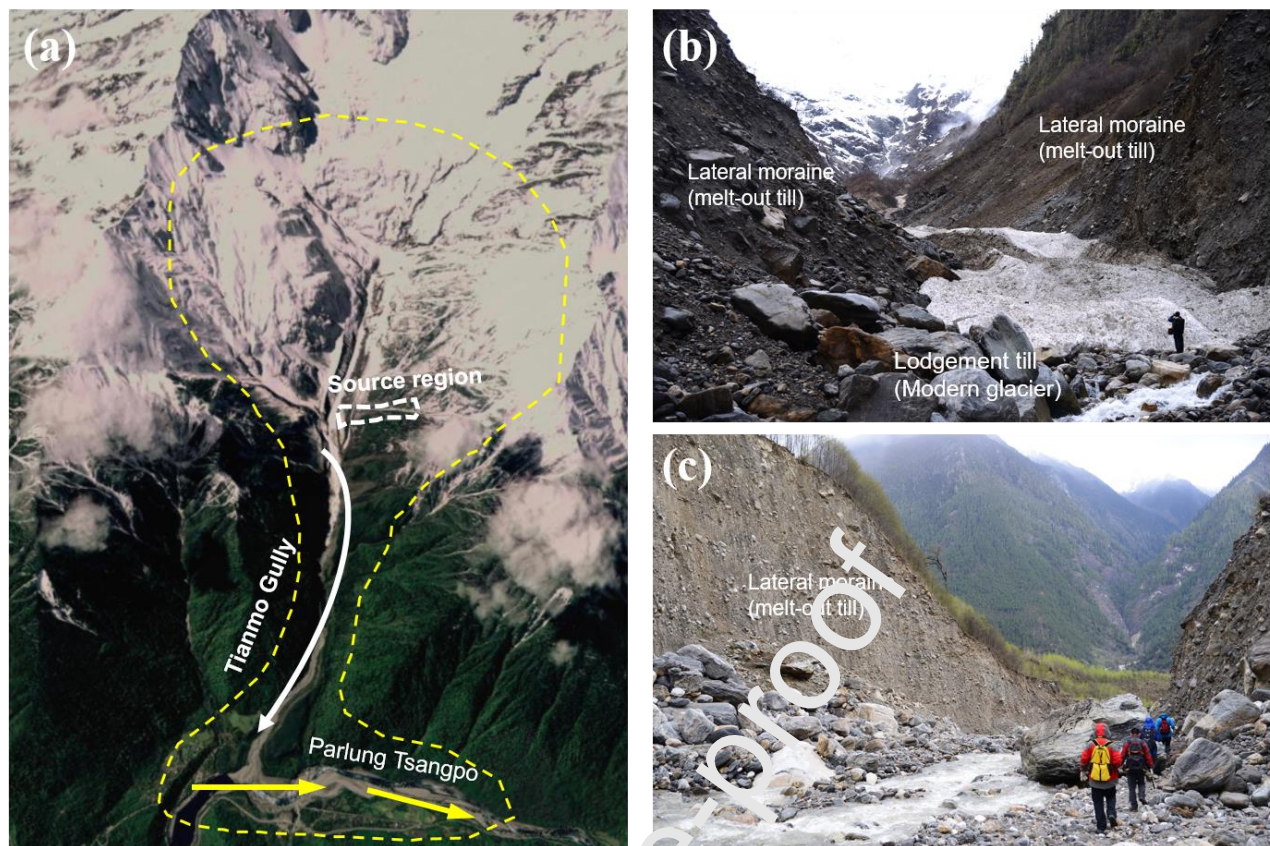


Fig. 9. (a) High-resolution satellite image of the Tianmo Gully, (b) the deposit profiles at the glacier tongue area, (c) the deposit profile of the lateral moraine.

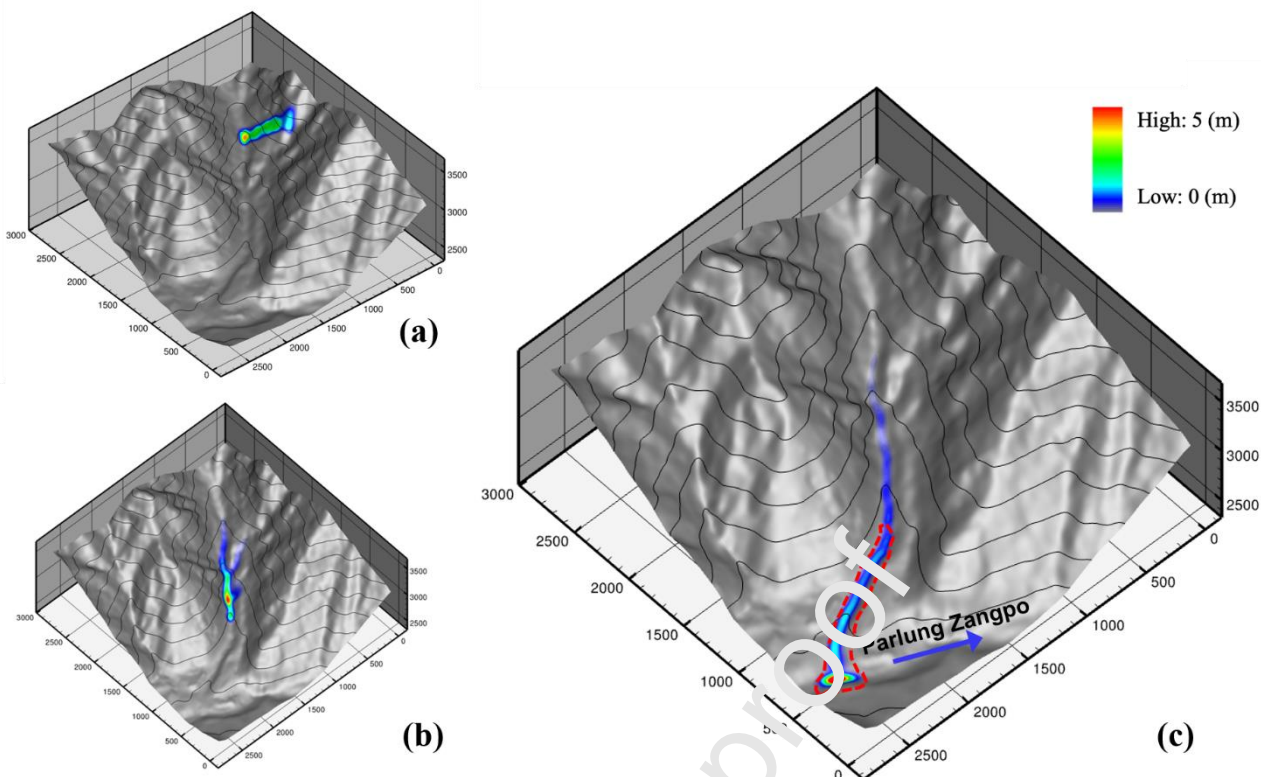


Fig. 10. (a-c) The total flow height profiles at time $t = 1.90, 180$ s respectively.

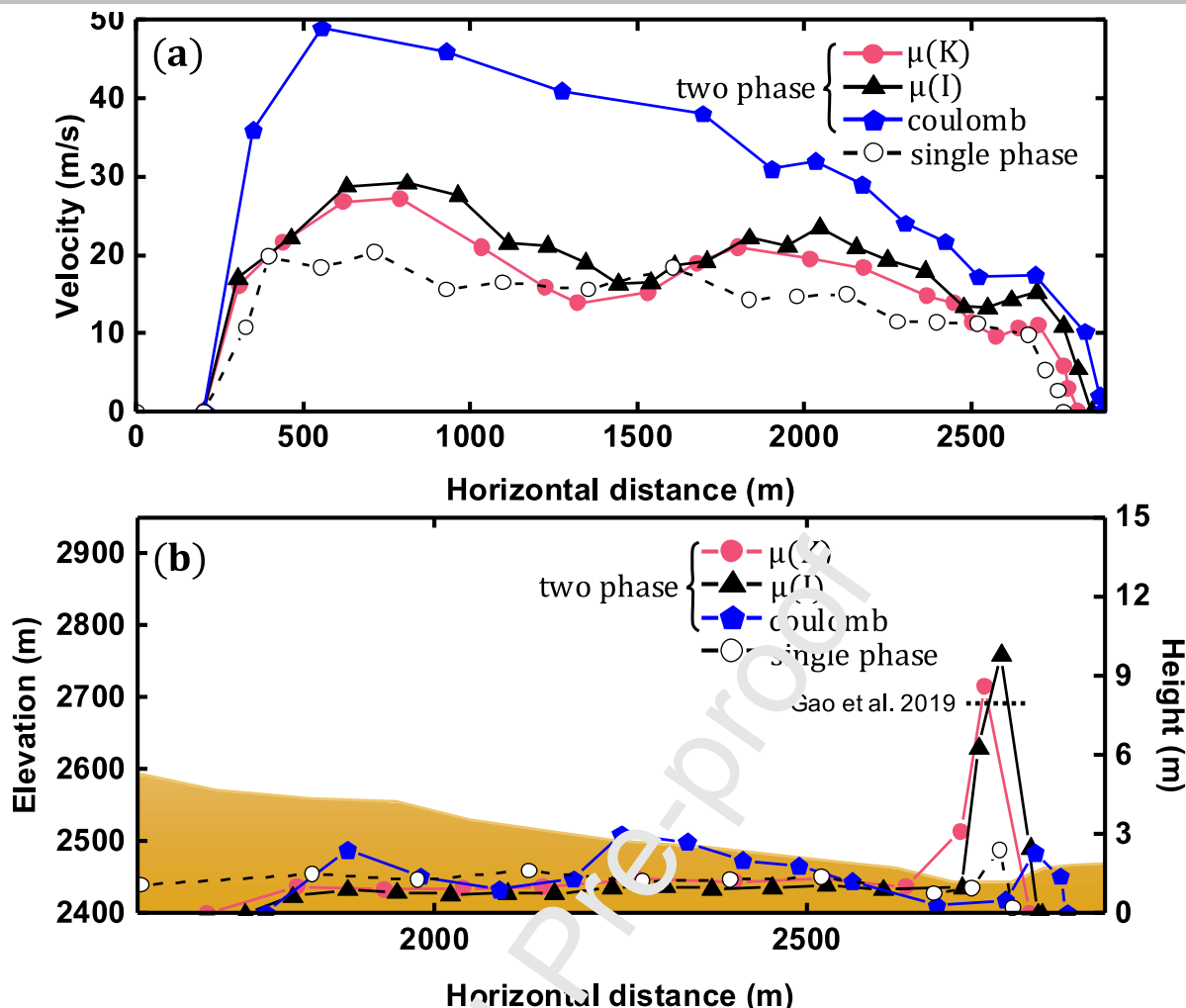


Fig. 11. (a-b) Velocity and height simulation profiles using different typical solid phase constitutive laws.

Author Statement

Manuscript: Numerical investigation of debris flows using a two-phase depth-averaged continuum model incorporating a visco-inertial rheology (No. ENGEO-D-21-01844)

The manuscript has not been previously published and is not currently submitted for review to any other journal. It will not also be submitted elsewhere before one decision is made.

All authors made significant contributions to the paper and have expressed their approval for its submission on their behalf.

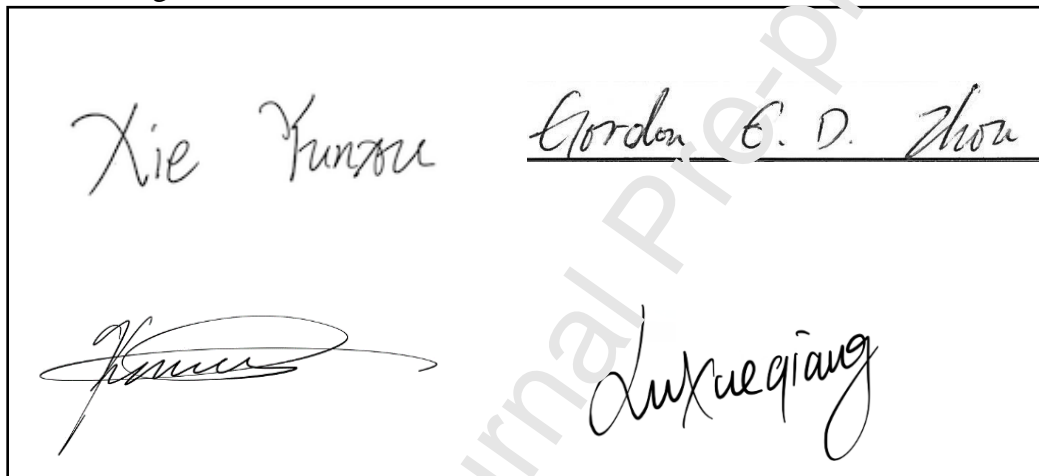
Yunxu Xie made substantial contributions to the methodology, supervision, and writing -Original draft preparation.

Gordon G. D. Zhou made substantial contributions to the conception, validation, project administration, and funding acquisition.

Kahlil F. E. Cui made substantial contributions to the reviewing, editing, and polishing.

Xueqiang Lu made substantial contributions to the initial discussion.

Author signature:



Declaration of interests

- The authors declare that they have no known competing financial interests or personal relationships that could have appeared to influence the work reported in this paper.
- The authors declare the following financial interests/personal relationships which may be considered as potential competing interests:

Xie Yunru

Gordon G. D. Zhou

Kahlil Fredrick E. Cui

Aixueqiang

Highlights:

- Debris flows are simulated as two-phase flows where the solid phase is modelled using a visco-inertial constitutive rheology.
- The numerical model captures the enhanced mobility and phase separation in debris flows.
- Simulations with visco-inertial model improves predictions against dry granular flow rheology.

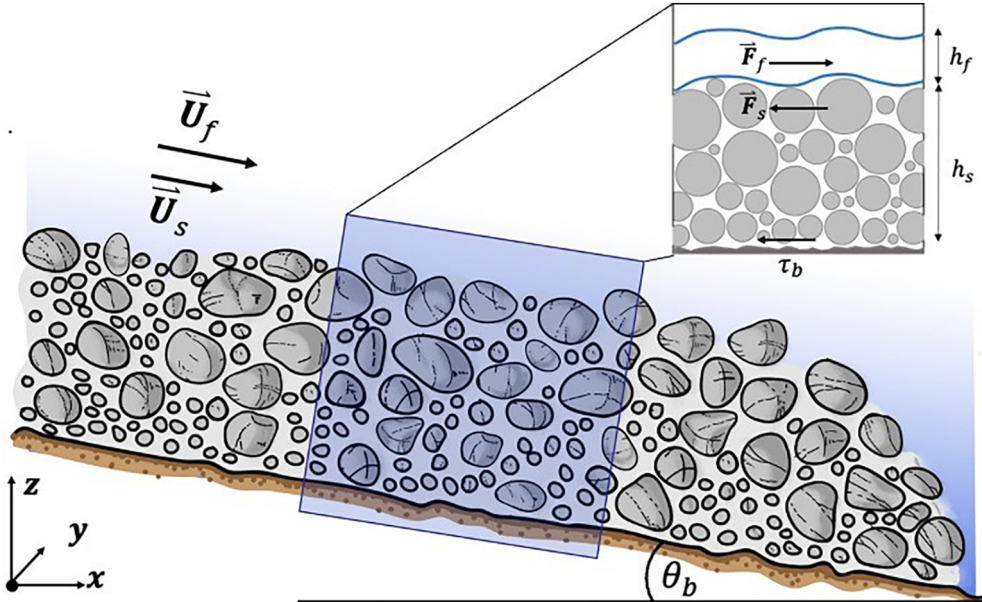


Figure 1

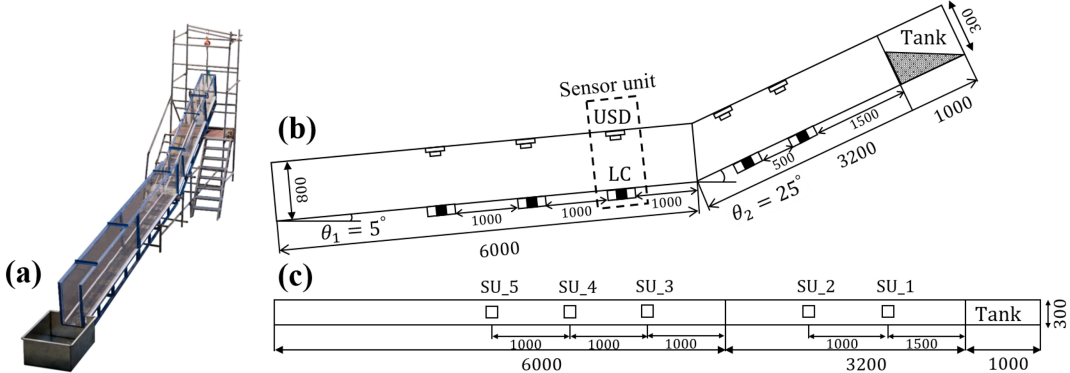


Figure 2

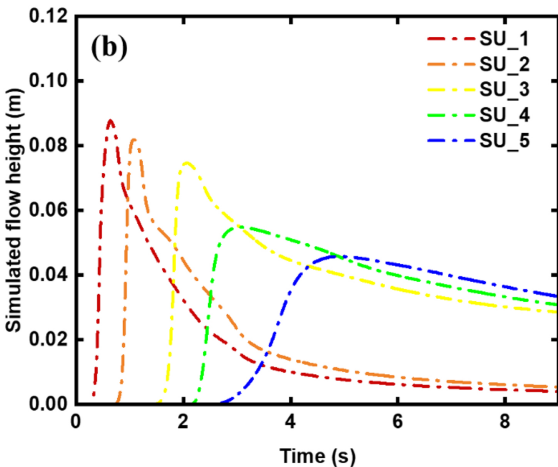
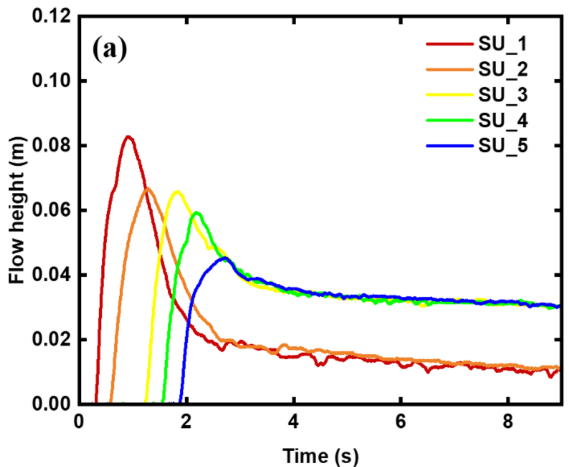


Figure 3

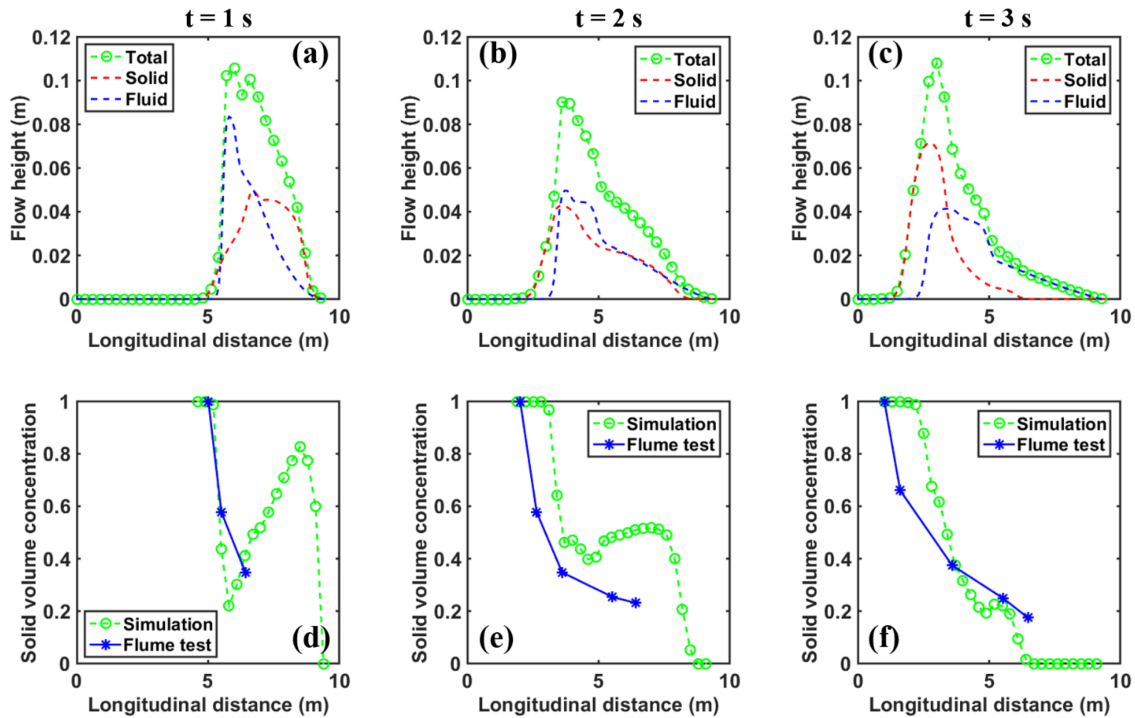


Figure 4

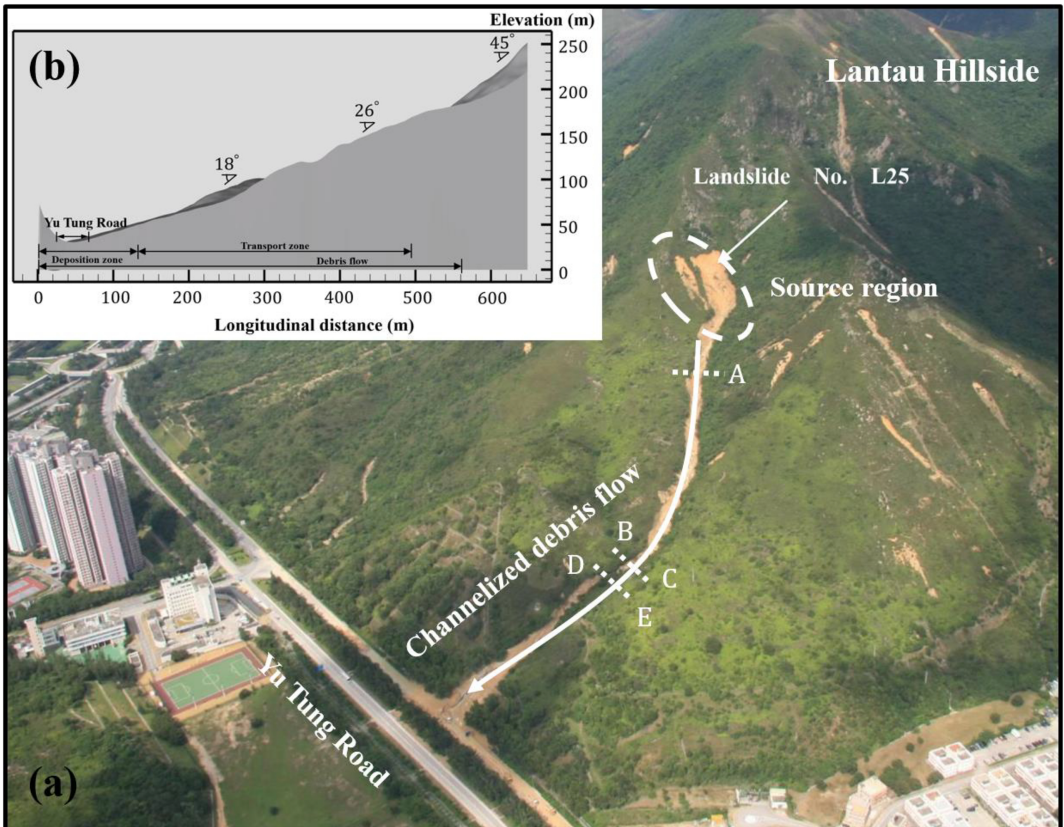


Figure 5

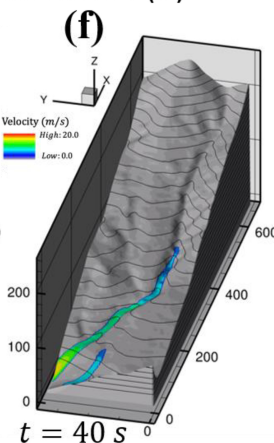
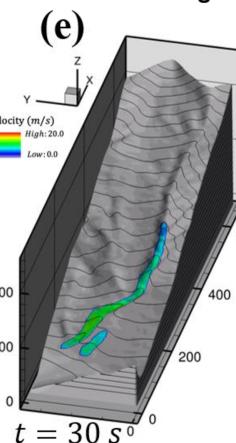
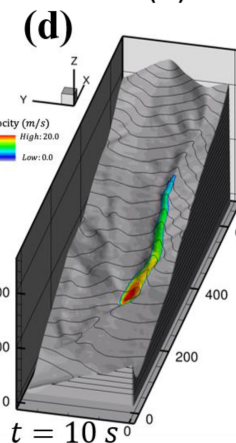
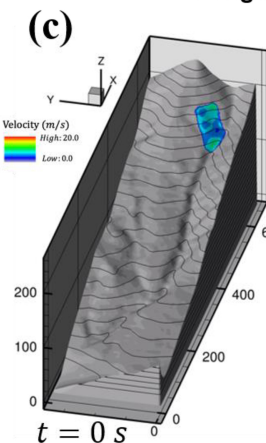
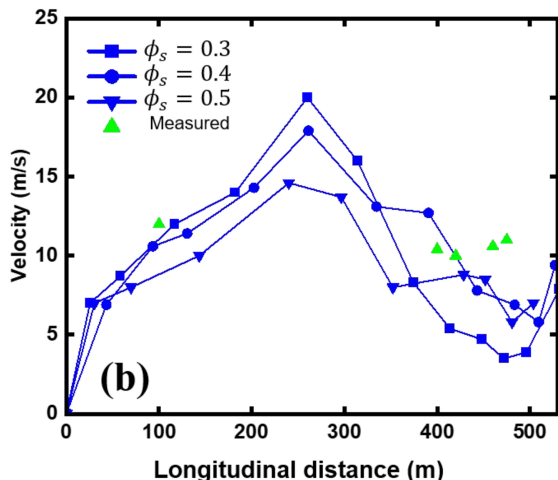
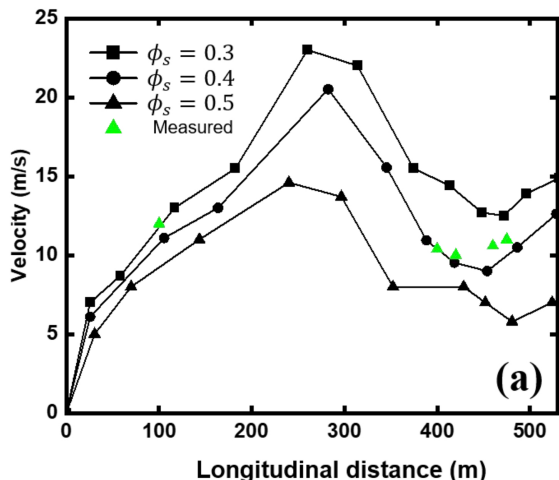


Figure 6

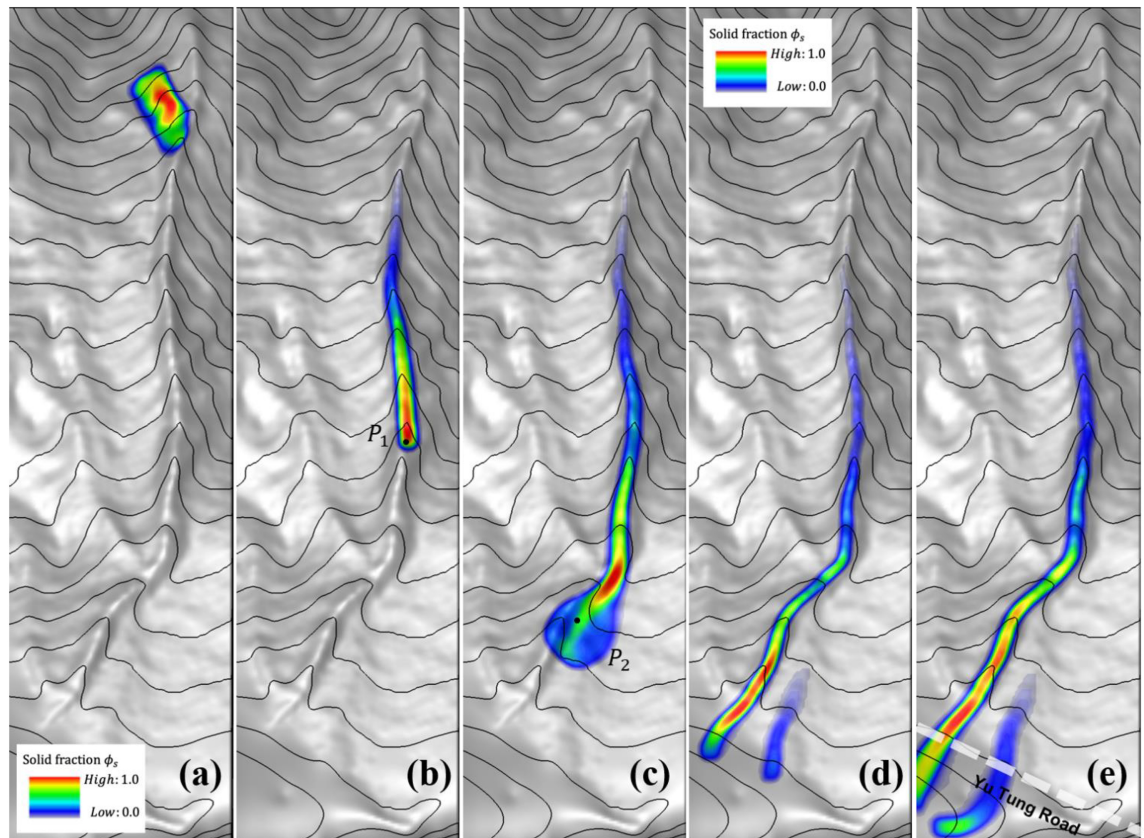


Figure 7

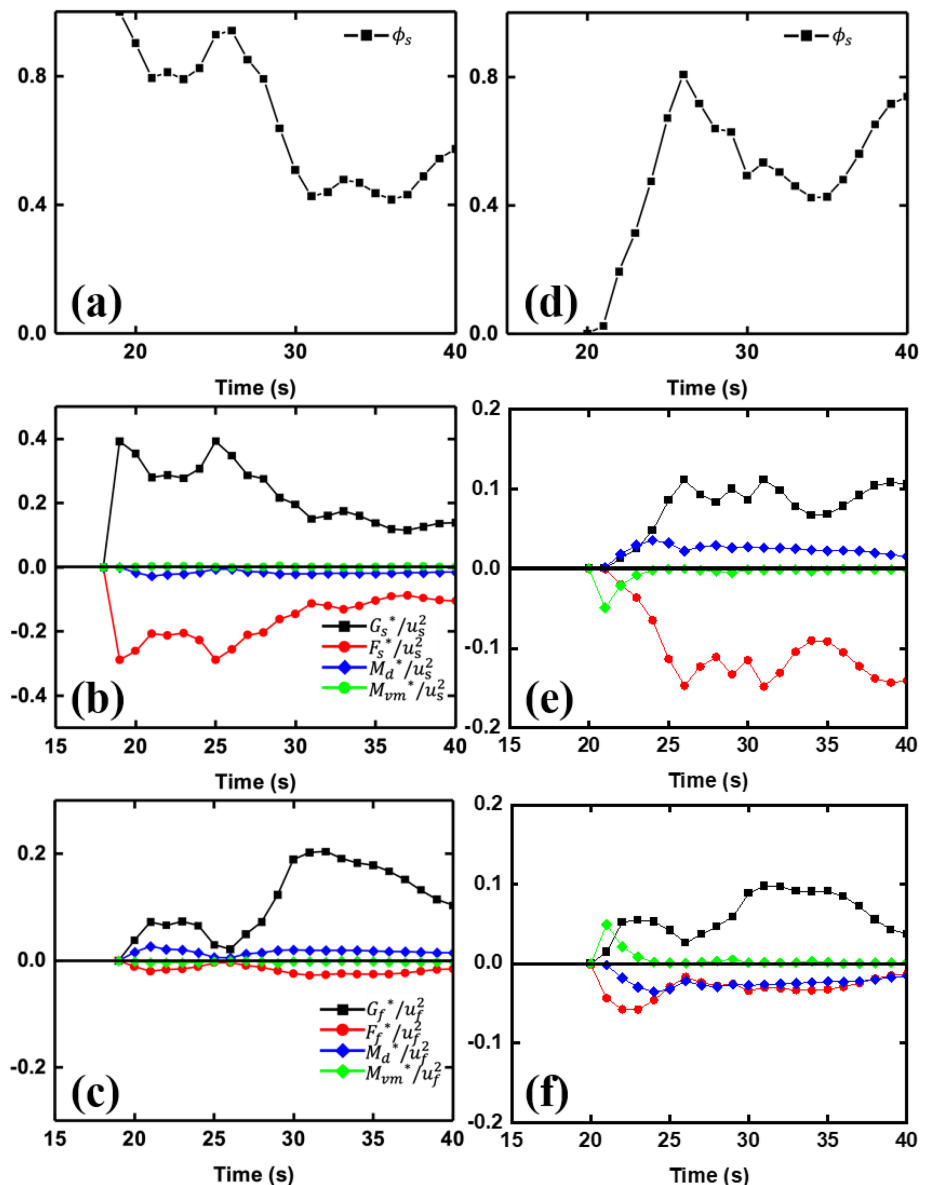


Figure 8

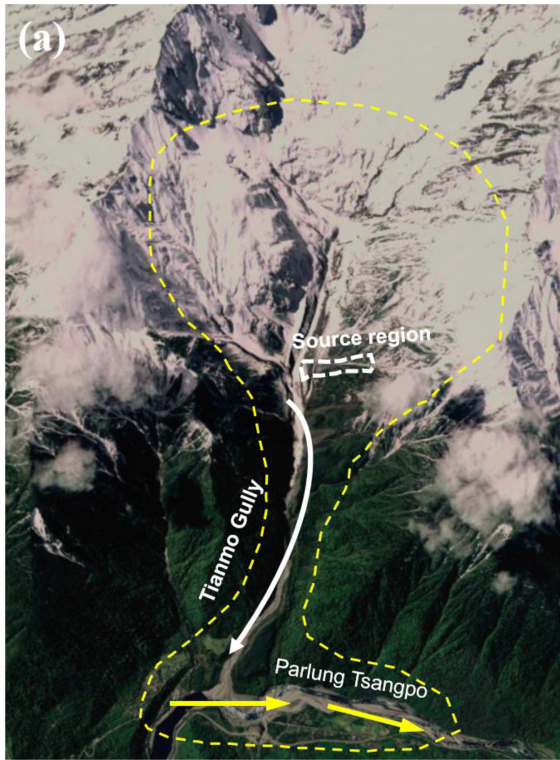
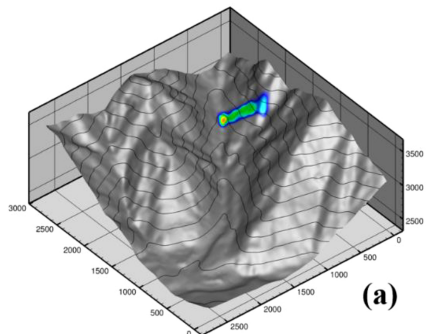
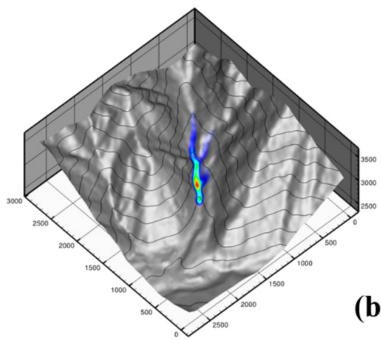


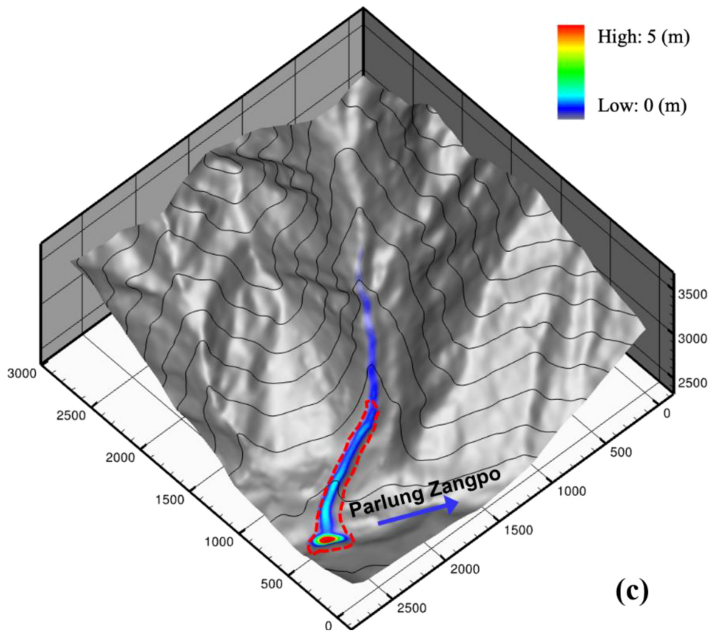
Figure 9



(a)



(b)



(c)

Figure 10

High: 5 (m)
Low: 0 (m)

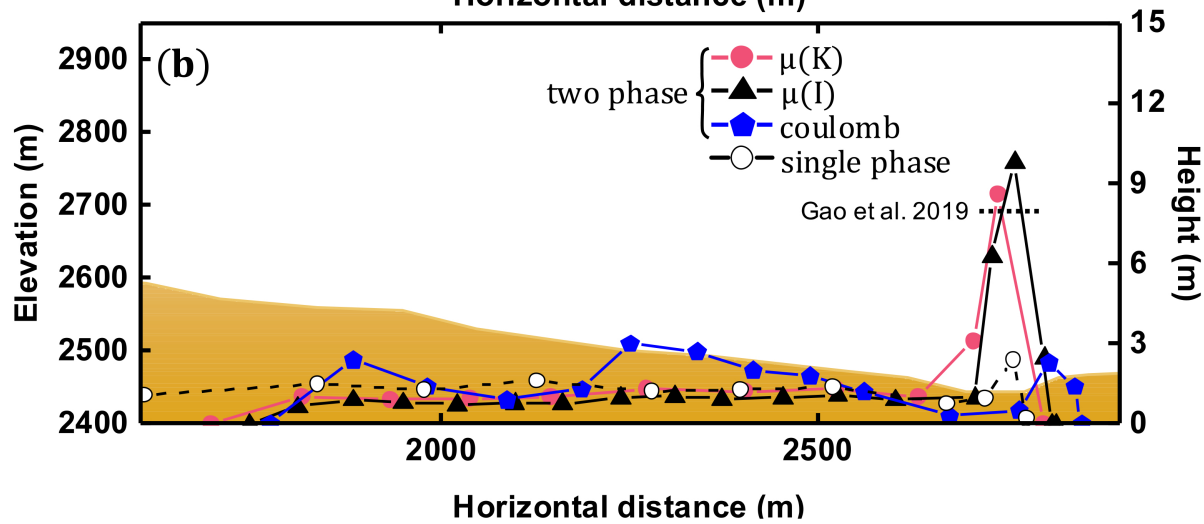
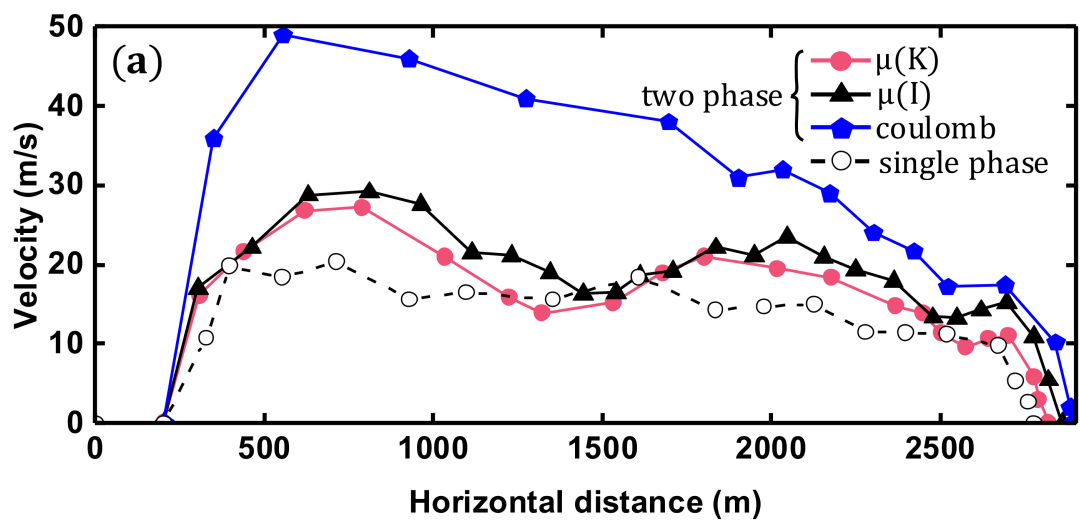


Figure 11